Master Thesis

Facile One-Step Deposition of Nanosized $Ni(OH)_2$-MoS_2 Heterostructure Electrodes for Efficient Oxygen Evolution Reaction

University of Ulsan

School of Mechanical Engineering

ROY DEEPTO

May 2023

효율적인 산소 발생 반응을 위한 나노크기 $Ni(OH)_2$-MoS_2 헤테로구조 전극의 손쉬운 1 단계 증착

Facile One-Step Deposition of Nanosized $Ni(OH)_2$-MoS_2 Heterostructure Electrodes for Efficient Oxygen Evolution Reaction

지도교수 천두만

이논문을 공학석사 학위 논문으로 제출함

2023 년 05 월

울산대학교 대학원 기계공학과

ROY DEEPTO

Facile One-Step Deposition of Nanosized $Ni(OH)_2$-MoS_2 Heterostructure Electrodes for Efficient Oxygen Evolution Reaction

A Thesis

Submitted to the School of Mechanical Engineering and the Graduate School of the University of Ulsan, Republic of Korea in partial fulfillment of the requirements for *the degree of Master of Science in Mechanical Engineering*

By

ROY DEEPTO

This certifies that the thesis of Deepto Roy has been approved.

This certifies that the thesis of Deepto Roy has been approved.

Thesis Committee Chairman **Professor BoHung Kim**

Thesis Committee Member **Professor Yoon Ho Lee**

Thesis Committee Member **Professor Chun Doo-Man**

The Graduate School

University of Ulsan

May 2023

ACKNOWLEDGEMENTS

I would like to express my deepest gratitude to my advisor, Professor Doo-Man Chun, for his great support, and guidance and for providing me with an excellent atmosphere for doing research. I am a novice in conducting research. I can learn how to conduct research from him with his constant supervision. It is a great understatement to say that this work would not have been accomplished without his help. I thank him for his excellent effort and patience with me to train me.

My sincere thanks to my colleagues in the hybrid manufacturing technology laboratory, especially Dr. Ahmed & Mr. Shehroze, who supported me a lot from the beginning of my journey. The outstanding friendly nature inside the laboratory helps me incredibly to do research.

Best regards,

Roy Deepto

May24’2023

Ulsan, South Korea

ABSTRACT

The growing demand for clean and sustainable energy sources relies on efficient and cost-effective electrocatalysts for the OER, a key energy conversion and storage device process. Using a vacuum kinetic spray technique nano-sized Ni $(OH)_2$–MoS_2 nanocomposites (NCs) electrocatalysts on nickel foam are fabricated from the corresponding micron powder. The modified working electrodes by Ni $(OH)_2$-MoS_2 NCs were utilized for oxygen evolution reaction (OER) at different weight ratios of MoS_2 (25, 50, and 75 wt.%). The surface state of the electrode is examined using sensitive techniques such as X-ray diffraction (XRD), scanning electron microscopy (SEM), Raman spectroscopy, and X-ray photoelectron spectroscopy (XPS). SEM images showed that the microparticles were fragmented into smaller nanoscale particles. XPS spectra revealed the synergy enhancement in the Ni $(OH)_2$-MoS_2 NCs that resulted in a strong improvement in the OER activity, which hybrid NCs with 75 wt.% MoS_2 exhibits the lowest overpotential of 282 mV@10 $mA \cdot cm^{-2}$ and the lowest Tafel slope of 54 $mV \cdot dec^{-1}$. Besides, the long-term OER durability is verified up to 50 h.

Keywords: Vacuum kinetic spray, Nano-particle deposition system (NPDS), Thin film, Oxygen Evolution Reaction.

CONTENTS

ACKNOWLEDGEMENTS i

ABSTRACT ii

CONTENTS iii

LIST OF TABLE v

LIST OF FIGURES v

LIST OF ABBREVIATIONS v

CHAPTER 1 INTRODUCTION 1

1.1 Introduction to Electrocatalysis 1

1.2 Oxygen Evolution Reaction (OER) 2

1.3 Previous & Recent Trends of Electrocatalysts 3

1.4 Strategies to improve electrocatalytic activity. 4

1.5 Transition Metal-Based Materials & Heterostructure 6

1.6 Techniques for thin film fabrication 8

1.7 Objectives of this Research 9

CHAPTER 2 METHODOLOGY 11

2.1 Materials Selection 11

2.2 Experimental Setup 11

2.3 Summary of process parameters 13

2.4 Characterization of thin films 13

2.5 Electrocatalytic activity analysis 15

CHAPTER 3 ELECTROCATALYTIC RESULTS 17

3.1 Electrochemical active surface area 17

3.2 Electrocatalytic Activity of Heterostructure Electrode 18

CHAPTER 4 THIN FILM CHARACTERIZATION 23

4.1 Images of thin films 23

4.2 XRD ANALYSIS 23

4.3 SEM ANALYSIS 25

4.4 RAMAN ANALYSIS 29

4.5 XPS ANALYSIS 33

CHAPTER 5 CONCLUSION 39

ACKNOWLEDGEMENT 40

REFERENCES: 40

LIST OF TABLES

Table. 1 Process Parameters for Ni (OH)2-MoS2 Heterostructure on Nickel Foam…….....12

Table. 2 Values of h, Tafel slope, R_{ct}, and ECSA of the modified electrode with Ni$(OH)_2$-MoS_2 NCs at various MoS_2 contents.....20

Table. 3 Identification of active Raman modes in the nanostructured Ni $(OH)_2$-MoS_2 heterostructure electrodes at various MoS2 Content……30

Table 4 XPS peaks positions estimated from the deconvolution of XPS scans… 35

LIST OF FIGURES

Figure 1 Schematic presentation of Electrocatalysis.....3

Figure 2 Techniques to improve electrocatalytic activity. 5

Figure 3 Objectives of this research. 10

Figure 4 Schematic for the vacuum kinetic spray method (NPDS) 12

Figure 5 OER LSV curve (a), Tafel plots (b), Nyquist Plot(c), current density vs scan rate in non-faradic region 18

Figure 6 Stability test for 50 hours(a), LSV curve after the stability test (b).....21

Figure 7 Deposited thin films. 23

Figure 8 XRD patterns of Ni (OH)2-MoS2 composites in powder form (a) and thin film deposited on nickel foam (b) 24

Figure 9 SEM images of Ni $(OH)_2$ Powder (a, b), MoS_2 Powder (c, d),75% MoS_2 (e, f) 27

Figure 10 SEM images of Ni $(OH)_2$/NF (a, b), MoS_2/NF (c, d),75% MoS_2/NF (e, f).....28

Figure 11 Raman Spectra of powder and thin film respectively. Ni $(OH)_2$ (a, b), MoS_2(c, d),75% MoS_2 (e, f)..... 30

Figure 12 Deconvoluted Mo 3d XPS scan of pure MoS_2 (a), 75 % MoS_2 heterostructure 34

Figure 13 Deconvoluted Ni 2p XPS scan of Pure Ni $(OH)_2$(a), 75% MoS_2 heterostructure(b)..... 35

Figure 14 Deconvoluted O 1s XPS scan of pure Ni $(OH)_2$ (a), 75%MoS_2(b) 36

Figure 15 Deconvoluted S 2p XPS scan of pure MoS_2 (a), 75 % MoS_2 heterostructure thin film (b) 37

LIST OF ABBREVIATIONS

Sl. No.	Short Form	Full Form
1	NPDS	Nano-particle deposition system
2	SoD	Stand-off distance
3	Ni $(OH)_2$	Nickel Hydroxide
4	MoS_2	Molybdenum Sulphide
5	NF	Nickel Foam
6	XRD	X-Ray Diffraction
7	SEM	Scanning Electron Microscope
8	XPS	X-Ray Photoelectron Spectroscopy

CHAPTER 1

INTRODUCTION

1.1 Introduction to Electrocatalysis

Electrocatalysis is the use of catalysts to accelerate electrochemical reactions. It has various applications in different energy-related fields [1]. Due to climate change and the fast development of the global economy, energy has become a primary focus in the scientific and industrial communities. With concerns about environmental pollution, increasing mining costs, and the depletion of fossil fuel, there is an urgent need for an efficient, clean, and renewable energy source, and energy storage technique. Manufacturing effective energy conversion and storage devices are now a current concern [2-3]. Electrochemical reactions are the fundamental parts of these recent sustainable and renewable energy devices.

Electrocatalysis with Electrocatalyst materials is one of the promising research topics due to its numerous uses in various fields. The fields in which it has diverse applications have been stated below: [4-5]

- Energy conversion
- Energy storage
- Sensors
- Electrometallurgy
- Electrosynthesis

1.2 Oxygen Evolution Reaction (OER)

Electrochemical reactions involve oxidation and reductions which depend on the efficient electron transfer, and electroactive site to produce an efficient reaction mechanism. Electrocatalytic Oxygen Evolution (OER) is one of the electrocatalysis processes (regarded as water electrolysis or water splitting) and numerous new electrocatalysts have been developed to improve the efficiency of gas evolution. In **Figure 1**, schematic presentations of the electrocatalysis have been shown [4]. Among the electrocatalysis reactions, the oxygen evolution reaction (OER) is often regarded as the main bottleneck in water splitting due to its slow kinetics, which limits the efficiency of the energy conversion, and further study is required [5]. The reactions are mostly stable in an alkaline medium. The chemical reaction for efficient oxygen evolution reaction is stated below: [6]

$$OH^- \longrightarrow *OH + e^-$$

$$*OH \longrightarrow *O + H^+ + e^-$$

$$*O + OH^- \longrightarrow *OOH + e^-$$

$$*OOH \longrightarrow O_2 + H^+ + e^-$$

Here, OH^- first undergoes concerted oxidative adsorption on the surface. The adsorbed *OH then undergoes oxidative deprotonation to form *O. Then, *O reacts with another OH− to form an *OOH intermediate. In the final step, *OOH is deprotonated to evolve O_2 with the regeneration of the active site. This four-electron transfer process can be combined and expressed as the following reaction.

$$4OH^- \longrightarrow \rightarrow O_2 + H_2O + 4e^-$$

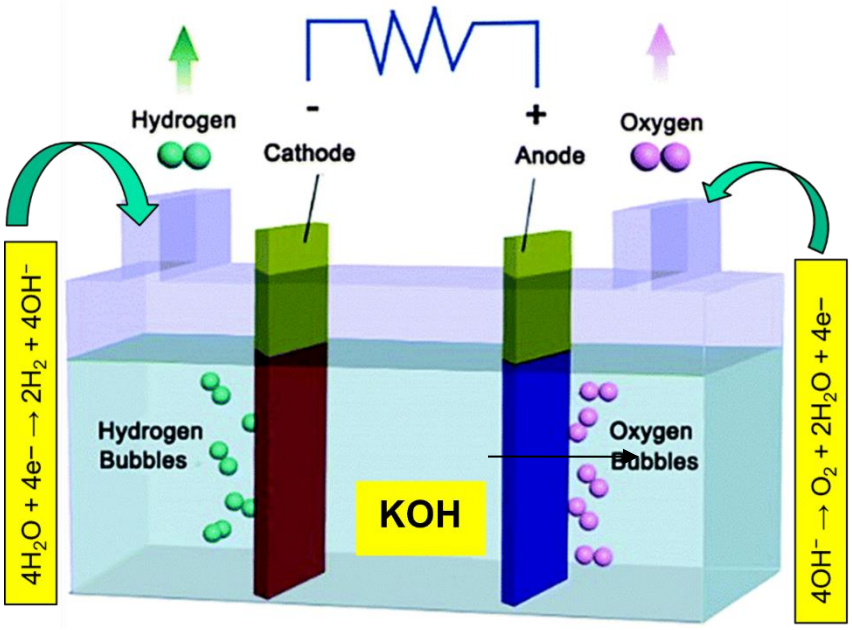

Figure 1 schematic presentation of Electrocatalysis

1.3 Previous & Recent Trends of Electrocatalysts

Electrocatalysis is a crucial component of various electrochemical systems used for energy storage and conversion applications, such as metal-air batteries, CO_2 reduction, and water splitting [9-10]. For efficient electrocatalysis, electrocatalysts play a major role in improving the sluggish reaction kinetics. Noble metal-based electrocatalysts such as IrO_2 and RuO_2, are severely limited by the high cost and low earth abundance of these noble metals. Transition metal-based electrocatalysts based on oxides, hydroxides/oxyhydroxides, chalcogenides, nitrides, and phosphides are great options because of their low price and abundance. They possess high electrocatalytic activity because of the high concentration of electroactive sites and efficient charge transfer networks through specific morphologies. Though these non-noble metal OER electrocatalysts may suffer from poor conductivity and inferior long-term durability [11-14].

1.4 Strategies to improve electrocatalytic activity.

Many strategies have been adopted to improve the electrocatalytic process for individual electrocatalysts. Surface modifications, doping with other materials, composite formation, and formation of multilayers are the most common strategies shown in **Figure 2** to improve electrocatalytic performance.

One potential approach to enhance the efficiency of electrocatalysts involves the utilization of nanostructures inspired by natural forms such as flowers and tubes, which can be employed to modify the surface of the electrocatalyst. This modification aims to reduce charge transfer limitations and increase catalytic activity, ultimately resulting in improved performance [15-16]**.**

In the quest for improved electrocatalytic performances, researchers like Zhu et. al [17] and Cheng et. al [18] have explored the use of two-dimensional (2D) layered materials. These materials can be employed either at the interface of double-layered hydroxides or as a single electrocatalyst. Examples of such 2D materials include graphene, graphitic carbon nitride, transitional metal dichalcogenides, and MXenes. The incorporation of 2D materials is particularly advantageous due to their higher charge transportation capability and the presence of active sites, making them a focal point of current research endeavors.

Additionally, Doping, another technique employed by certain researchers [19-20], offers a means to enhance wettability, conductivity, and local charge distribution, which are crucial factors for achieving efficient electrocatalysis. Furthermore, the creation of heterostructures or composites is a widely employed strategy for developing efficient electrocatalysts. By forming these composite

structures, synergistic improvements can be achieved on the catalyst surface. Promising results have been reported by researchers such as Hameed et. al [21], Zhang et. al [22], who have successfully demonstrated enhanced performance using composite electrocatalysts.

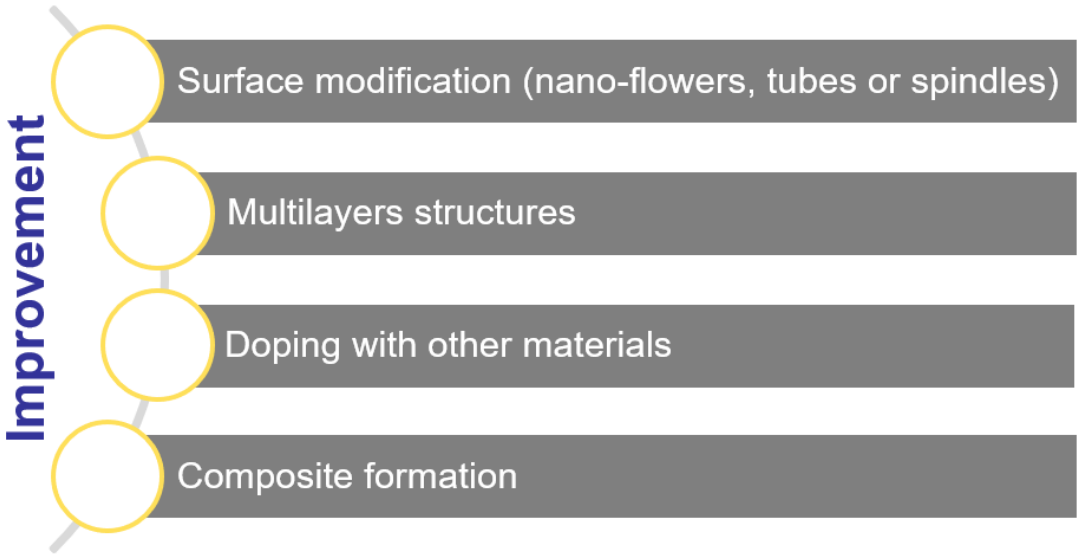

Figure 2 Techniques to improve electrocatalytic activity.

1.5 Transition Metal-Based Materials & Heterostructure

Ni $(OH)_2$ is a first-row transition metal-based hydroxide that shows promising performances regarding energy-based devices with different morphology and architecture [23]. For example, Kim et. al proposed that β-Ni $(OH)_2$ nanoplates containing many oxygen vacancies fabricated by a hydrothermal method and achieved a low overpotential of 340 mV and a current density of 10 $mA \cdot cm^{-2}$ [24]. However, its application is limited because of the poor conductivity and insufficient exposure of active sites [25]. To overcome this, Guo et. al synthesized hollow nanorod arrays of Ni $(OH)_2$ on Nickel foam through alkali etching and coated the hollow walls with electrodeposited FeOOH [26]. Nanostructured MoS_2 electrocatalysts are frequently utilized for water-splitting applications because of their layered structure, electronic band arrangement [27-28], and the presence of electro-catalytic active sites at interfacial and defect-rich edges [29– 30]. However, it suffers from a significant obstacle regarding initiating water dissociation and reaction intermediates in water splitting [31]. To improve the water dissociation and adsorption of reaction intermediates, hybridization, alloying, doping, and many more efforts have been taken on MoS_2 [32-33].

Among certain methods, interface engineering has yielded highly effective techniques for significantly improving the electrochemical performance of electrocatalysts. The interface of heterostructures exhibits electronic, morphologic, coordination, and synergistic integration effect [34]. Creating heterostructure electrodes is an effective method for altering the surface structure of the working electrode, which leads to the generation of high concentrations of interfacial electroactive sites. Alongside this, developing new heterostructures can facilitate cooperation between electroactive species that reduce the overpotential energy barrier in the initial step of water dissociation and favor the optimum adsorption of the reaction intermediates [35-37].

Chen et. al. [38], have fabricated $NiSe_2$ and $FeSe_2$ heterostructure through a facile and scalable method on nickel-iron foam. This interface lowers the Gibbs free energy of reaction intermediates which explicitly affects the reduction of energy barrier height. Guan et. al. used a three-step technique to construct a core-shell structure on nickel foam with MoS_2/NiS & Ni_3S_2 and achieved high catalytic performances fast charge transfer kinetics and durability[39]. Wen et. al. formulated MoS_2/NiS_2 electrocatalyst for Lithium oxide batteries which illustrated superior performances due to d band modification and electronic interactions on the heterostructure interface. These modifications served to adjust the adsorption energy of oxygen intermediates [40]. Zhang et. al exploited a perovskite-based $NiRuO_3$ structure formed between NiO & Ru interface. They used a two-step deposition method to induce better hydrophilicity and lower charge transfer properties that enabled them to fabricate an efficient electrocatalyst with a cell voltage of 1.55 eV at 10 $mA{\cdot}cm^{-2.}$ [41]. Si et al. utilized a doping strategy through a template-confined approach to co-dope MoS_2 nanosheets with Co and Fe, which led to an increase in the electroactive surface area of the electrode as well as the improvement of charge transfer [42]. $Ni(OH)_2$-MoS_2 nanocomposites (NCs) are a promising electrocatalyst for energy conversion applications including water splitting. Wang at. el. fabricated hierarchical and self-supported electrodes for water electrolysis in alkaline media by decorating 1T phase MoS_2 nanowire with Ni $(OH)_2$ nanoparticles. It improved electrocatalytic activity due to the energy barrier reduction of the our-step electron transfer process [43]. Another study investigated by He et. al. illustrated a facile method to create a Ni $(OH)_2/MoS_2$ heterostructure that transformed into hydroxide active sites through penetration of Nickel into the irritated detect sites of MoS_2 [44]

1.6 Techniques for thin film fabrication

The effectiveness of Ni $(OH)_2$ and MoS_2 heterostructure as an electrocatalyst, the drawback may come to finding an efficient, easy-going, sustainable manufacturing process. Most synthetic methods are limited to small substrates due to the high costs and lengthy fabrication time required to produce nanopowder with binder attachment to the substrates to form the thin films. Moreover, hazardous chemical solutions have been used in most techniques that necessitate a prolonged and complex cleaning process for their removal and do not validate a sustainable production environment. For example, the utilization of gas phase-based physical and chemical vapor deposition techniques poses certain challenges, primarily in the form of relatively high operating temperatures ranging from 900K to 1500K, intricate gas phase sensitivity, and the vaporization of multicomponent materials due to varying vaporization temperatures. Furthermore, the elevated working temperatures can give rise to several oxidation and reduction reactions on the surface, which can impede the growth of the thin film. Chemical solution-based synthesis techniques, such as Sol-gel, hydrothermal, and solvothermal synthesis, entail a complex synthesis mechanism, which results in high costs and prolonged processing times. Additionally, controlling the microstructure and growth of the thin film through this convoluted procedure can be challenging [45-46]. Solution-based spray & spin coating is widely used in the thin film synthesis process though surface roughness and uniformity in large-scale and curved surfaces is still a limiting factor [47]. Furthermore, the electrodeposition technique is a low costing process with low-level control parameters for nanoparticles, nanorods, nanowires, and nanoclusters synthesis. However, it requires a conductive surface to be used as a substrate, and non-uniformity nucleation growth & contamination through solvents is still a challenge [48-49]. In contrast to the above-mentioned conflicts, a top-down

nanoparticle deposition (NPDS) technique facilitates fragmentation and exfoliation of the layer of microparticles into nano sizes through high-velocity impacts with a hard metallic sheet. This process is preferable due to its deposition capability at room temperatures, binderless thin film formation, no extra hazardous chemical involvement, and large-scale production capability. During the deposition process, there is no destruction or damage due to local thermal heating. It is a time-saving one-step facile nano thin film synthesis process from micronized powder.

1.7 Objectives of this Research

In this study, Ni $(OH)_2$ powders with different MoS_2 (0 - 100 wt.%) were deposited on Nickel Foam by NPDS. The electrocatalytic activity of thin films was assessed, and the kinetic behavior of the reaction was studied. The thin films were characterized by X-ray diffraction (XRD), field emission scanning electron microscopy (FE-SEM), X-Ray Photoelectron Spectroscopy, and Raman spectroscopy.

The objectives of this research are:

1. To fabricate thin films for clean energy technology through an eco-friendly fabrication process.
2. To manufacture efficient electrodes for Oxygen Evolution Reaction (OER) at room temperature and in a time-efficient manner.
3. To study the composition ratio effect for efficient Oxygen Evolution Reaction.

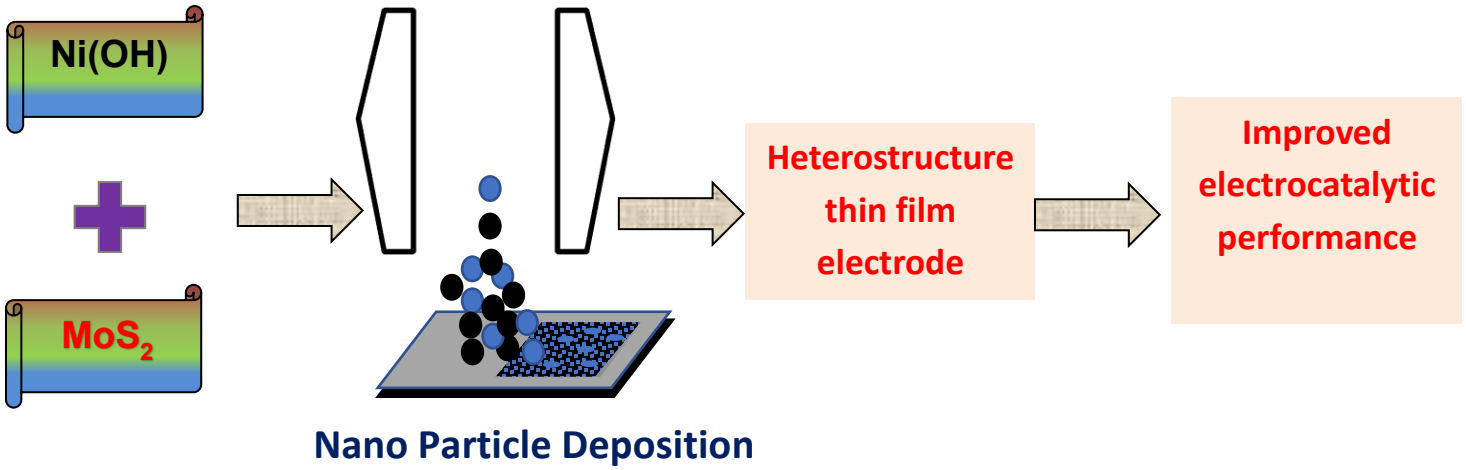

Figure 3 Objectives of this research.

CHAPTER 2

METHODOLOGY

2.1 Materials selection

The deposition of nano-sized heterostructure electrodes required the use of high-quality initial sources. To this end, MoS_2 microparticles, sourced from Sigma-Aldrich in the USA with an average size of 2.5 μm with a 98% assay (CAS No: 1317-33-5), were employed alongside micron-scale powders of Ni $(OH)_2$ (CAS No: 12054-48-7, sourced from Sigma-Aldrich). The deposition was carried out on open-cell NF porous substrates (measuring 1.6 mm in thickness, with a density of 350 g/m^2, and 110 pores per inch, sourced from Invisible Inc. in Korea). To study the OER, a 1.0 M KOH electrolyte from Daejung in Korea (CAS#1310-58-3) was used.

2.2 Experimental setup

Firstly, micro-sized Ni $(OH)_2$ & MOS_2 powders were weighed together at a ratio of 100:0, 75:25, 50 and:50, and 25:75 by precise measurement with a weight measuring machine. The weighted powders were then mechanically mixed via a ball mill machine with 12h and 600 rpm. After that, Ni $(OH)_2$ & MOS_2 powders with different graphite contents were deposited on Nickel foam by kinetic spraying. The NPDS consists of a compressor to supply compressed air, a cylinder-piston type powder feeder, a vacuum pump, a nozzle, and a controller, as shown in **Figure 5**.

The powders stored in the cylinder come to the brush chamber section when the piston moved up. The high rotational speed of the brush drives the powders into the mainstream of pressurized carrier gas coming from an air compressor. The pressurized carrier gas can easily carry the powders to a converging nozzle where it sprays the powders onto the substrate at high-speed utilizing the pressure difference between compressed air and vacuum. The powders utilizing kinetic energy can easily be fragmented and deposited on Nickel Foam. A suitable SoD, i.e., the distance between the substrate and nozzle is maintained for this research because the deposition behavior also depends on SoD. The thin films were prepared within a very short time. The prepared films were immediately cleaned by air cleaning. The films were then kept in a clean place to use for the electrocatalytic oxygen evolution reaction.

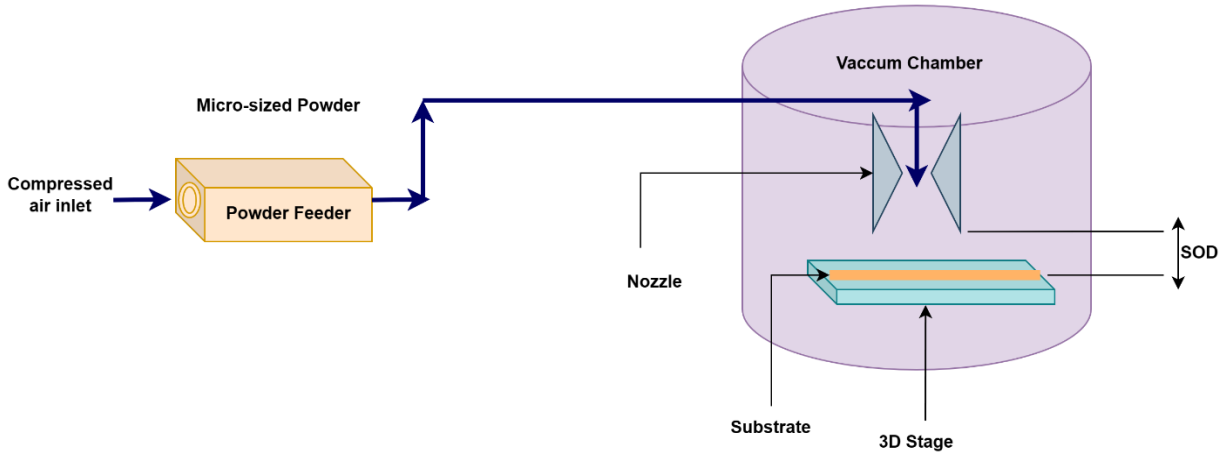

Figure 4 Schematic for the vacuum kinetic spray method (NPDS)

2.3 Summary of process parameters

Process parameters are very important in depositing with the vacuum kinetic spray method. No parameter has not been changed during the whole experiment. Complete constancy of parameters was maintained for Ni $(OH)_2$ & MOS_2 deposition. **Table 1** gives detailed information about process parameters.

Table 1 Process parameters for Ni $(OH)_2$ & MoS_2 on NF substrate.

Parameters	**Value**
Air Pressure (bar)	3.5
Chamber pressure (Torr)	390-420
Distance between substrate and nozzle (mm)	5.0
Stage speed (rpm)	375
Piston speed (rpm)	3000
Piston bore diameter (mm)	14
Brush speed (rpm)	8000
Deposition area (cm × cm)	4 × 4
Nozzle dimension (mm × mm)	5 × 0.4

2.4 Characterization of thin films

SEM uses a condensed, accelerated electron beam to focus on a specimen. The electron beam hits the specimen and produces secondary and backscattered electrons. Secondary electrons are emitted from the sample and collected to create an area map of the secondary emissions. Since the intensity of secondary emission is very dependent on local morphology, the area map is a magnified image of the sample.

In this thesis work, SEM images were measured by scanning electron microscopy (JSM-6500F, Jeol, Japan)

X-ray diffraction (XRD) takes advantage of the coherent scattering of X-rays by polycrystalline materials to obtain a wide range of structural information. The X-rays are scattered by each set of lattice planes at a characteristic angle, and the scattered intensity is a function of the atoms, which occupy those planes. The scattering from all the different sets of planes results in a pattern that is unique to a given compound. The peak of this pattern is formed when a constructive interference between the reflected x-rays by the atomic planes takes place satisfying Bragg's law ($n\lambda=2d \sin \theta$) satisfied where λ is the x-ray wavelength, d is the spacing distance and θ diffraction angle. The crystallite size can be calculated using the Scherrer equation:

$$D=\kappa\lambda cos$$

where κ is a constant (usually = 0.9), and β is the full width at half maximum intensity (FWHM)[93]. In the thesis crystalline structure was identified using X-ray diffraction Ultima IV, Rigaku, Japan (Cu Kα radiation, λ=0.15418nm) operated at 40 kV and 30 mA.

Raman spectroscopy is a spectroscopic technique used to study vibrational, rotational, and other low-frequency modes in a system. It relies on inelastic scattering or Raman scattering of monochromatic light, usually from a laser in the visible, near-infrared, or near-ultraviolet range. The laser light interacts with phonons or other excitations in the system, resulting in the energy of the laser photons being shifted up or down. The energy shift gives information about the phonon modes in the system. In this thesis work, the Raman spectra were carried out using Raman spectroscopy (Alpha 300R, WITec, Germany) with a 532 nm wavelength laser operating at 1 mW as an excitation source.

The chemical state of a sample is analyzed by X-ray Photoelectron Spectroscopy (XPS). An electron is emitted by the photoelectric effect when homogeneous light is applied to the material. The measuring method of electron energy and intensity distribution is called the XPS method.

$$E_{kin} = hv - E_b - \varphi$$

where E_{kin} is the kinetic energy of emitted photoelectron, hv is the incident X-ray energy, E_b is the binding energy of the emitted electron, and φ is the work function for the sample. If hv is constant, binding energy can be obtained by measuring the kinetic energy of the emitted electron. Identification of elements is easily possible by measuring E_{kin} because the binding energy of each electron orbit is different. On the other hand, the binding energy of the same orbit of the same element is changed a little by an atomic surrounding state and environment. A state analysis of an element is possible by measuring this change variation called chemical shift. X-ray photoelectron spectroscopy was performed with a K-alpha XPS system (Thermo Fisher Scientific, Waltham, MA, USA).

2.5 Electrocatalytic activity analysis

$$E_{RHE} = E_{Hg/HgO} + E^{o}_{Hg/HgO} + 0.059 * pH \qquad (1)$$

The present study examined the electrocatalytic activity of Ni foam-modified working electrode with $Ni(OH)_2$, MoS_2, and heterostructures $Ni(OH)_2$-MoS_2 NCs towards OER in a 1.0 M KOH solution using a 3-electrode cell configuration and an electrochemical workstation (C350, Wuhan Corr-test Instruments Corp. Ltd., Wuhan, China). The working electrodes had a geometrical area of 1 cm^2, while a Pt mesh served as the counter electrode, and a Hg/HgO electrode in 1.0 M KOH was

used as a reference electrode. All potentials were adjusted for IR and calibrated to RHE using the following equation.

The standard potential of $E^{o}_{Hg/HgO}$ concerning RHE is 0.098 V, while $E_{Hg/HgO}$ represents the applied potential difference relative to Hg/HgO. Linear sweep voltammetry (LSV) plots were obtained by scanning from 0.276 to 0.876 V vs. Hg/HgO at a scan rate of 5 mV/s to record the OER in 1.0 M KOH with a pH of 14. The OER Overpotential can be calculated from the following equations.

$$\eta_{OER} = E_{OER} - E^{o}_{OER} - IR \qquad (2)$$

In this context, E^{o}_{OER} refers to the potential of the working electrode, while E_{OER} is the standard potential of OER (1.23 V vs. RHE). Additionally, R denotes the resistance of the electrolyte between the reference electrode and the working electrode surface, which was determined by measuring the Nyquist plots using electrochemical impedance spectroscopy (EIS) at the high-frequency region where the imaginary part of the impedance (Z″) is zero. The real part of the impedance (Z′) corresponds to R, which is then multiplied by the given current density (IR) according to Eq. (2) to obtain an accurate value of h for the OER in 1.0 M KOH.

The Tafel equation was utilized to analyze how the electrochemical reaction rates varied. The slope obtained through the use of Eq. (3) reflects the electrochemical reaction kinetics of the modified electrode consisting of nanostructured composites of $Ni(OH)_2$-MoS_2 structure.

$$\eta = b\log\left(\frac{j}{j_o}\right) \qquad \mathbf{(3)}$$

CHAPTER 3

ELECTROCATALYTIC RESULTS

3.1 Electrochemical active surface area

The electrochemical active surface area (ECSA) of $Ni(OH)_2$, MoS_2, and $Ni(OH)_2$-MoS_2 NCs were calculated through the interfacial capacitance of the electric double layer of the electrode-electrolyte interface. The potential is linearly scanned in the non-faradic region from 0 to 0.1 V vs. Hg/HgOin 1.0 M KOH electrolyte.

$$\Delta J = Janode - Jcathode = C_{DL}\vartheta \quad (4)$$

This term C_{DL} indicates the slope of the linear relationship between the current density (J) and the scan rate for a given current density.

A linear relationship based on Eq. (4) between anodic and cathodic current difference (current density J) vs scan rate (ϑ) has been presented in **Figure 5(d).** The estimated C_{DL} refers to the ECSA v for the fabricated heterostructure electrodes. The three heterostructures with different compositions present improvement where 75% MoS_2 shows the highest though the ECSA improvement is slightly higher compared to the basic Ni $(OH)_2$ & MoS_2 phases. The ECSA value of the pure phases of $Ni(OH)_2$ and MoS_2 are 3.00 $mF.cm^{-2}$ and 3.41 $mF.cm^{-2}$ respectively whereas the heterostructure electrodes with increasing MoS_2 content achieved ECSA values of 3.73, 4.1 & 4.3 $mF.cm^{-2}$.Therefore, the catalytic activity improvement may come from synergy improvement, however, may not be specifically from the improved active surface area [50-51]. Alongside, between the interface of two materials due to

synergy and electron interactions effect, interface engineering can provide better charge transfer kinetics which can be better for catalytic activity and can be confirmed with Impedance spectroscopy (EIS).

3.2 Electrocatalytic Activity of Heterostructure Electrode

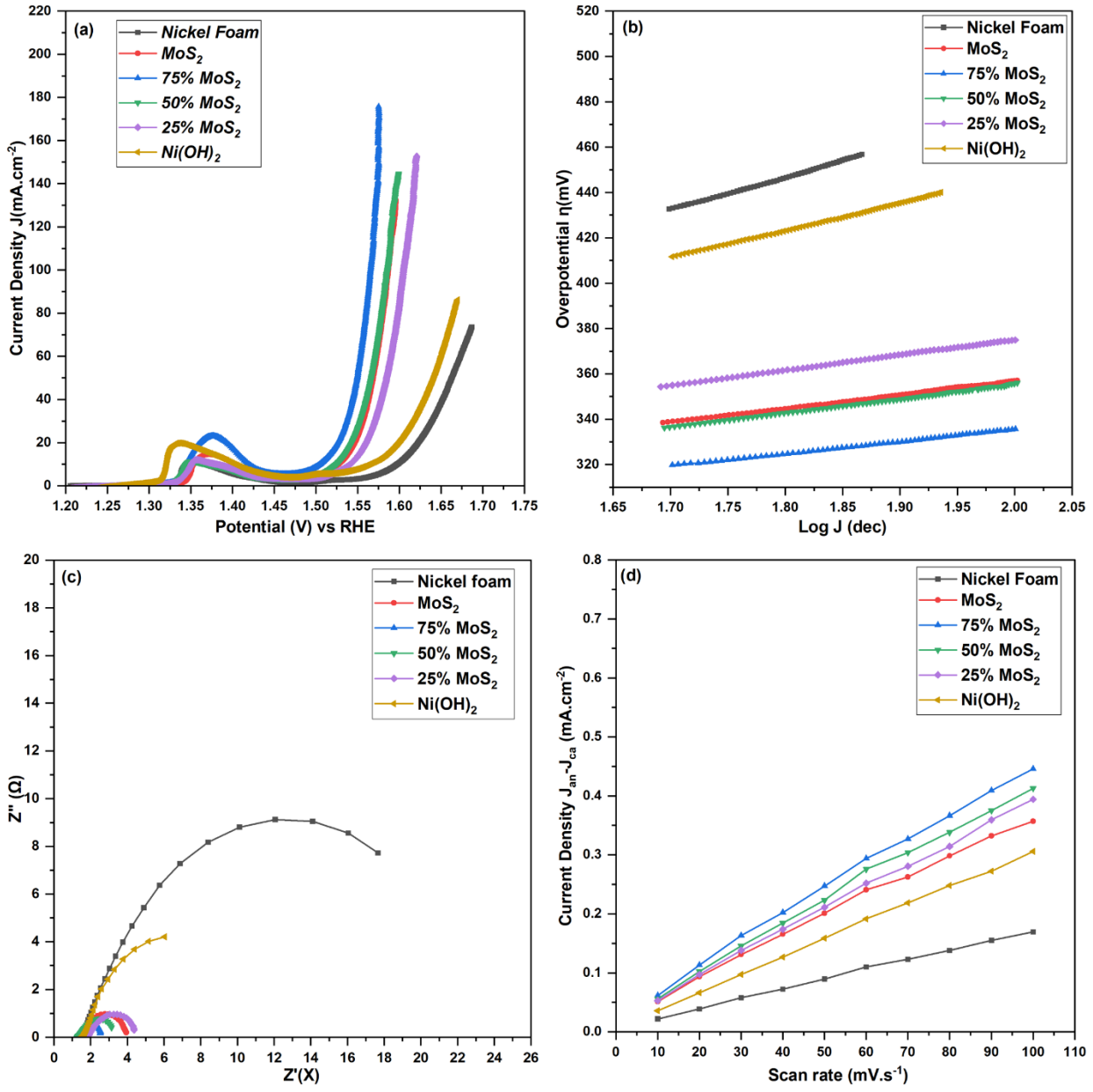

Figure 5 OER LSV curve (a), Tafel plots (b), Nyquist Plot(c), current density vs scan rate in non-faradic region

Figure 5 (a, b) provides the LSV curves and corresponding Tafel slopes of the Nickel foam, Ni $(OH)_2$ nanosheets, MoS_2 nanosheets, Ni $(OH)_2$-MoS_2 hybrid NCs with 25, 50, and 75 wt.% MoS_2. The potential range used for these electrochemical testing is between 1.2 to 1.8 V vs RHE in 1.0 M KOH as an electrolyte. The Ni $(OH)_2$ and MoS_2 exhibit overpotential (η) of 335 mV and 297 mV at 10 $mA{\cdot}cm^{-2}$, respectively. The $Ni(OH)_2$-MoS_2 NCs with 75 wt.% MoS_2 shows superior electrocatalytic activity by presenting lower η of 282 mV at 10 $mA{\cdot}cm^{-2}$ current density. The other two compositions of heterostructure electrode with 50% MoS_2 & 25% MoS_2 exhibits η of 294 mV and 306 mV respectively at 10$mA.cm^{-2}$ current density respectively.

The reaction rate is presented by the Tafel slope of the electrode. The reaction kinetics is very low for the Ni $(OH)_2$/NF and basic nickel foam electrode. To further improve it, the heterostructure electrode (75% MoS_2) has been deposited which presents a Tafel slope of 54 $mV.dec^{-1}$. The reaction rate is higher than basic MoS_2/NF electrode (60 $mV.dec^{-1}$) and indicates the optimum condition for the heterostructure electrode. The Tafel slope for the other two electrodes with Ni $(OH)_2$ higher percentage shows a slower reaction speed for OER than the basic MoS_2/NF phase. The two tafel slopes with 50% and 75% MoS_2 achieved tafel slopes of 63 & 70 $mV.dec^{-1}$ respectively. The lower conductivity of Ni $(OH)_2$ could be responsible for the slower reaction kinetics though they can provide superior electrocatalytic activity due to higher active sites. [52]

The transfer coefficient (α) is the equation that is used in the description of the kinetics o electrochemical reactions. The equation to calculate the α has been given below

$$\mathbf{1-\alpha=\frac{2.303*R*T}{b*n*F}} \quad (5)$$

Here, R is the gas constant, T is the absolute temperature,b is the Tafel slope,n is the participating electron in the reaction and F is the Faraday constant.The transfer coefficients of $Ni(OH)_2$,MoS_2, ,modified electrodes(75% MoS_2,50% MoS_2,25% MoS_2) are 0.87,0.75,0.72,0.77,0.79 respectively.

The charge transport resistance (R_{ct}) has been calculated from the Nyquist plot **(figure 5(c))**. The starting and ending frequency for the EIS measurement was 1000000Hz & 0.1Hz respectively for all the compositions. The peak intensity of frequency of the Nyquist plot for the pure phases and heterostructure electrodes has been written below. For the pure phases, $Ni(OH)_2$ & MoS_2 peak frequency was 0.16026 Hz & 1.3052 Hz respectively. The achieved peak frequencies for the heterostructure electrodes were 0.654 Hz,0.4076 Hz & 0.32328 Hz for the 75% MoS_2,50% MoS_2,25% MoS_2 respectively.

The charge transfer resistance is too high for the Nickel foam and Ni $(OH)_2$/NF electrode. MoS_2/NF can provide superior charge transfer kinetics which shows moderate charge transfer resistance of 4 $mF.cm^{-2}$ compared to the Nickel foam and Ni $(OH)_2$. The interface on the heterostructure composite with higher MoS_2 modifies the charge transfer resistance indicating the interfacial charge transfer improvement at the grain boundary of Ni $(OH)_2$-MoS_2. The modified electrode with 75% MoS_2 exhibits the lowest charge transfer resistance (2.3 mF/cm^2). However, the modified electrode dominated with Ni $(OH)_2$ (25% MoS_2) shows a little bit higher charge transfer resistance than the basic MoS_2/NF phase. These results suggest the superior effect of MoS_2 in heterostructure for charge transportation kinetics at the electrode/electrolyte interface and can be the fundamental factor for better electrocatalytic OER activity. Better electrocatalytic activity with increasing charge transfer can be explained with four electron transfer processes in the alkaline media described by Qiuhua et el. [53-54].

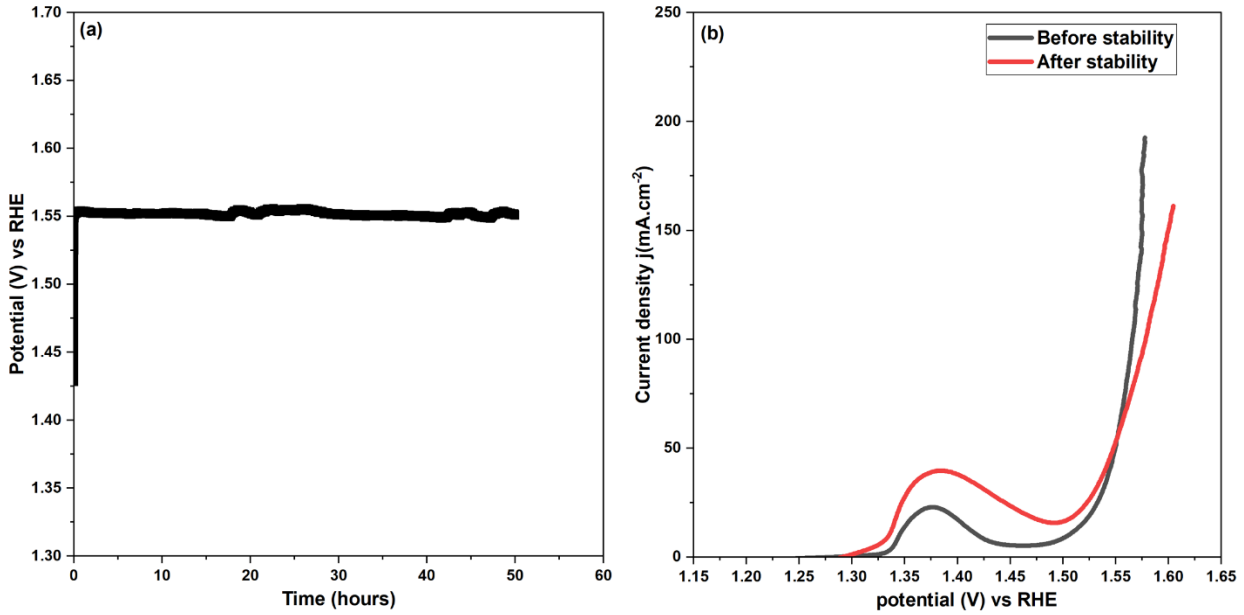

Figure 6 Stability test for 50 hours(a), LSV curve after the stability test (b)

Figure 6(a) illustrates the stability test that examines how well 75% MoS_2/NF remained stable in 1M KOH during bulk electrolysis with an initial current density of 50 mA/cm². The results show that the electrodes are remarkably stable for 50 hours, suggesting that the 75% MoS_2/NF electrode is both catalytically stable and mechanically strong. **Figure 6(b)** presents the OER LSV test after the stability test. It indicates that the OER overpotential produced a slight overpotential increase in higher currents. It proves that 75% MoS_2/NF is an efficient and stable electrode for Oxygen evolution.

Table 2: Values of h, Tafel slope, R_{ct}, and ECSA of the modified electrode with $Ni(OH)_2$-MoS_2 NCs at various MoS_2 contents.

Composition Ratio		**Overpotential (η) mcm^{-2}**				**Tafel slope ($made^{-1}$)**	**R_{ct} (Ω)**	**ECSA (mcm^{-2})**
Ni $(OH)_2$	**MoS_2**	10	20	50	100			
Bare Nickel foam		372	398	440	-	145	19.5	1.75
0	100	297	316	338	353	60	4.0	3.41
25	75	282	301	324	342	54	2.3	4.28
50	50	294	314	337	358	63	3.4	4.1
75	25	307	324	348	368	70	4.2	3.73
100	0	335	368	-	411	120	12.5	3.0

CHAPTER 4

THIN FILM CHARACTERIZATION

4.1 Images of thin films

The thin films of pure $Ni(OH)_2$, MoS_2, and composite were prepared by NPDS within a very short process time. To support thin films, Nickel Foam was used. After the fabrication of thin films, they were kept to use for electrocatalytic analysis.

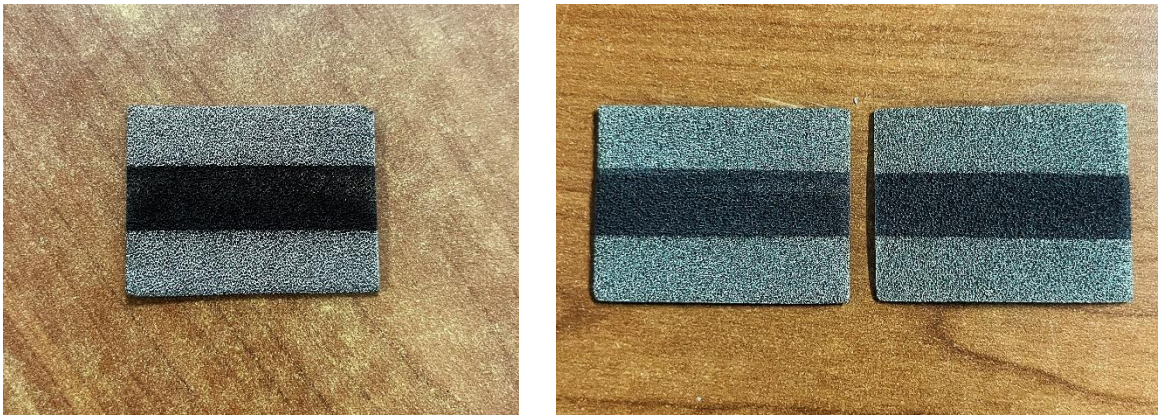

Figure 7 Deposited thin films.

4.2 XRD ANALYSIS

Figure 8(a) presents the XRD patterns of microcrystalline $Ni(OH)_2$, MoS_2, and a $Ni(OH)_2$-MoS_2 mixed powder containing 75 wt.% MoS_2. The XRD pattern of MoS_2 shows several characteristic peaks with relatively high intensity mixed with some other lower intensity. The recognized XRD peaks in pure MoS_2 powder are located at 14.48, 29.1, 32.82, 33.58, 35.98, 39.64, 44.24, 49.88, 56.14, 58.44, 60.36,

62.92, 66.62, 68.64, 70.26, and 72.68 correspond to the characteristic planes (002), (004), (100), (101), (102), (103), (006), (105), (106), (110), (008), (107), (114), (200), (108), and (203), respectively crystalline planes of bulk hexagonal MoS_2 phase species (space group: P63/MMC, ICDD: 30-065-1951, PDF 2010). In the case of pure Ni $(OH)_2$ micro-sized powder the identified peaks are at 19.06, 33.14, 38.52, 51.94, 59.12, 62.72, 69.52, and 72.76 ° corresponding to the (001), (100), (101), (102), (110), (111), (200), and (201) crystalline planes of hexagonal $Ni(OH)_2$ phase (space group: P-3m1, 00-014-0117, PDF 4+).

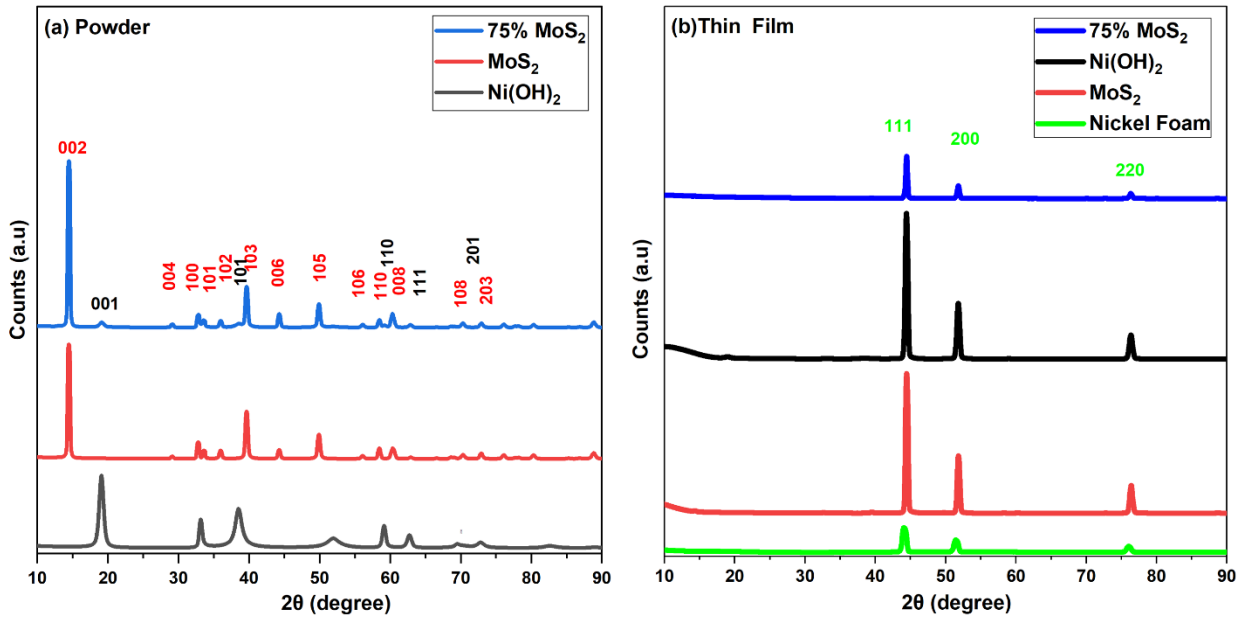

Figure 8 XRD patterns of Ni $(OH)_2$-MoS_2 composites in powder form (a) and thin film deposited on nickel foam (b)

XRD of Ni $(OH)_2$-MoS_2 composites with 75 wt.% MoS_2 By ball milling before deposition, 75% MoS_2 composed of both phases, reveals the presence of both phases hexagonal Ni $(OH)_2$ and hexagonal MoS_2 by comparing the peaks positions of pure phases. However, some peaks of pure phase powder have almost close diffraction

peaks in the case of Ni $(OH)_2$ & MoS_2. As a result, these peaks cannot visualize properly for the composite powder between these peaks.

Figure 8(b) illustrates XRD patterns of bare nickel foam, $Ni(OH)_2$ film, MoS_2 films, as well as $Ni(OH)_2$-MoS_2 NCs with 75 wt.% MoS_2. Three main diffraction peaks are observed in the case of bare Ni foam at 2θ values of 44.19, 51.54, and 76.09. These peaks correspond to the (111), (200), and (220) crystalline planes of the face-centered cubic structure of the pure nickel phase. From the XRD analysis of the nanostructured thin film, it is evident that the deposited film on nickel foam of Ni $(OH)_2$, MoS_2, and Ni $(OH)_2$-MoS_2 NCs with 75 wt.% MoS_2 only shows the characteristic peaks of bare nickel foam. However, other characteristic peaks of the base material Ni $(OH)_2$ and MoS_2 are also present there. A magnified view of the XRD graphs can confirm the clear characteristic peaks of base material phases Ni $(OH)_2$ and MoS_2. The Ni foam substrate used here is responsible for this behavior due to its high crystalline content. Furthermore, all deposited films show a low intensity of XRD peaks, suggesting that the microparticles are fragmented into smaller nanocrystalline domains. We can observe this behavior during the deposition of functional material through the NPDS technique**.**[55-56]. However, regarding Ni $(OH)_2$, only a peak at 19.24 ^{o} can be seen after more magnification. A lower percentage compared to MoS_2, higher fragmentation and huge size reduction during the deposition process is responsible for this. SEM and images, Raman spectroscopy can further illustrate the same phenomenon of extensive size reduction relative to MoS_2.

4.3 SEM ANALYSIS

In **Figure 9(a, b),** Ni $(OH)_2$ micropower shows different sizes of microparticles with non-uniform size distribution. The size varies by several micrometers. **Figure**

9(c, d) exhibits the surface morphology of MoS_2 micro-flakes with a stacked layered structure, which presents different multilayer sheet sizes ranging from 1 micron to certain micrometers. The composite Powder of the 75% MoS_2 (**figure 9(e,f))** shows the combination of Ni $(OH)_2$ microparticle and multilayer MoS_2 micron-sized particle.

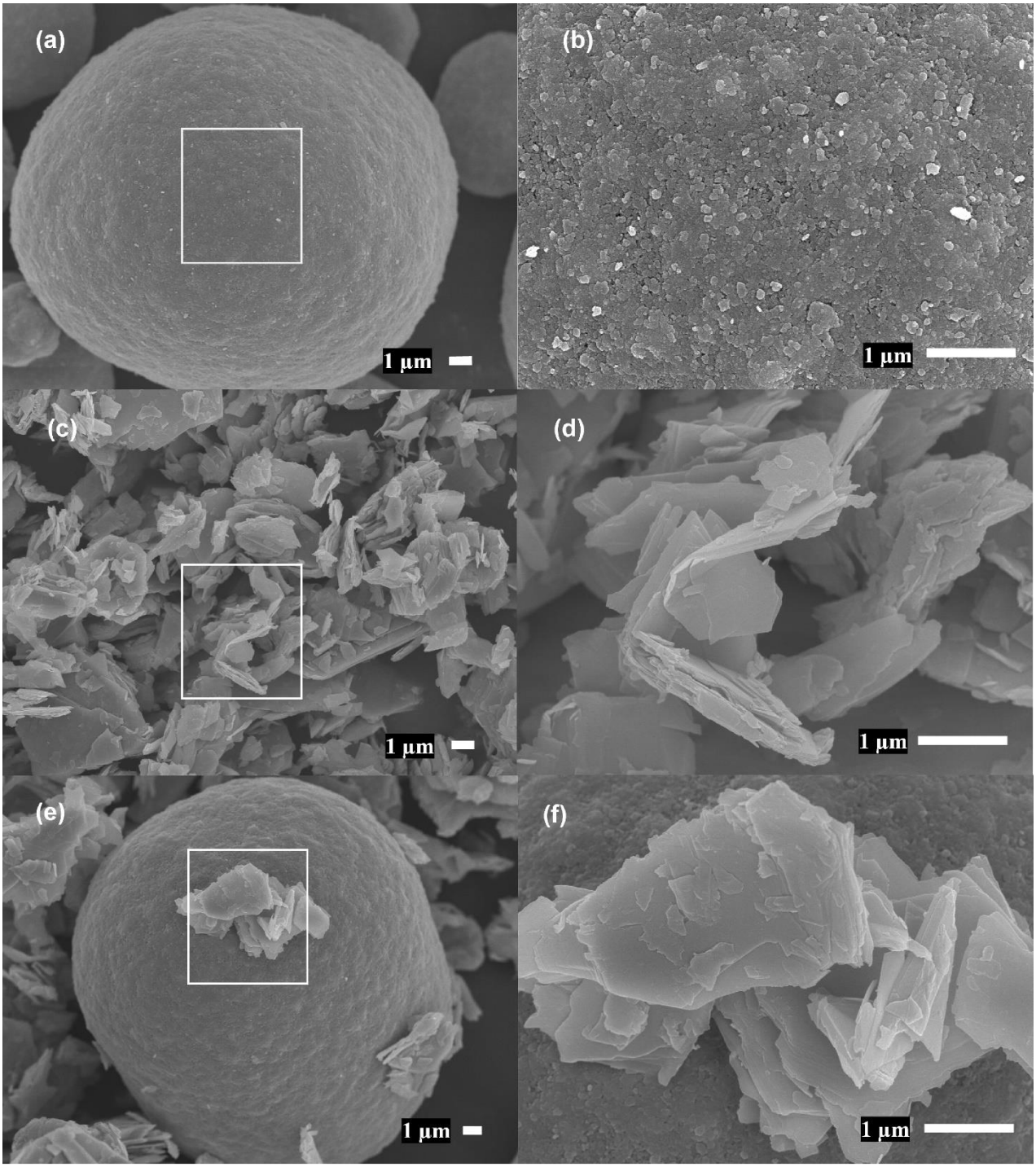

Figure 9 SEM images of Ni $(OH)_2$ Powder (a, b), MoS_2 Powder (c, d),75% MoS_2 (e, f)

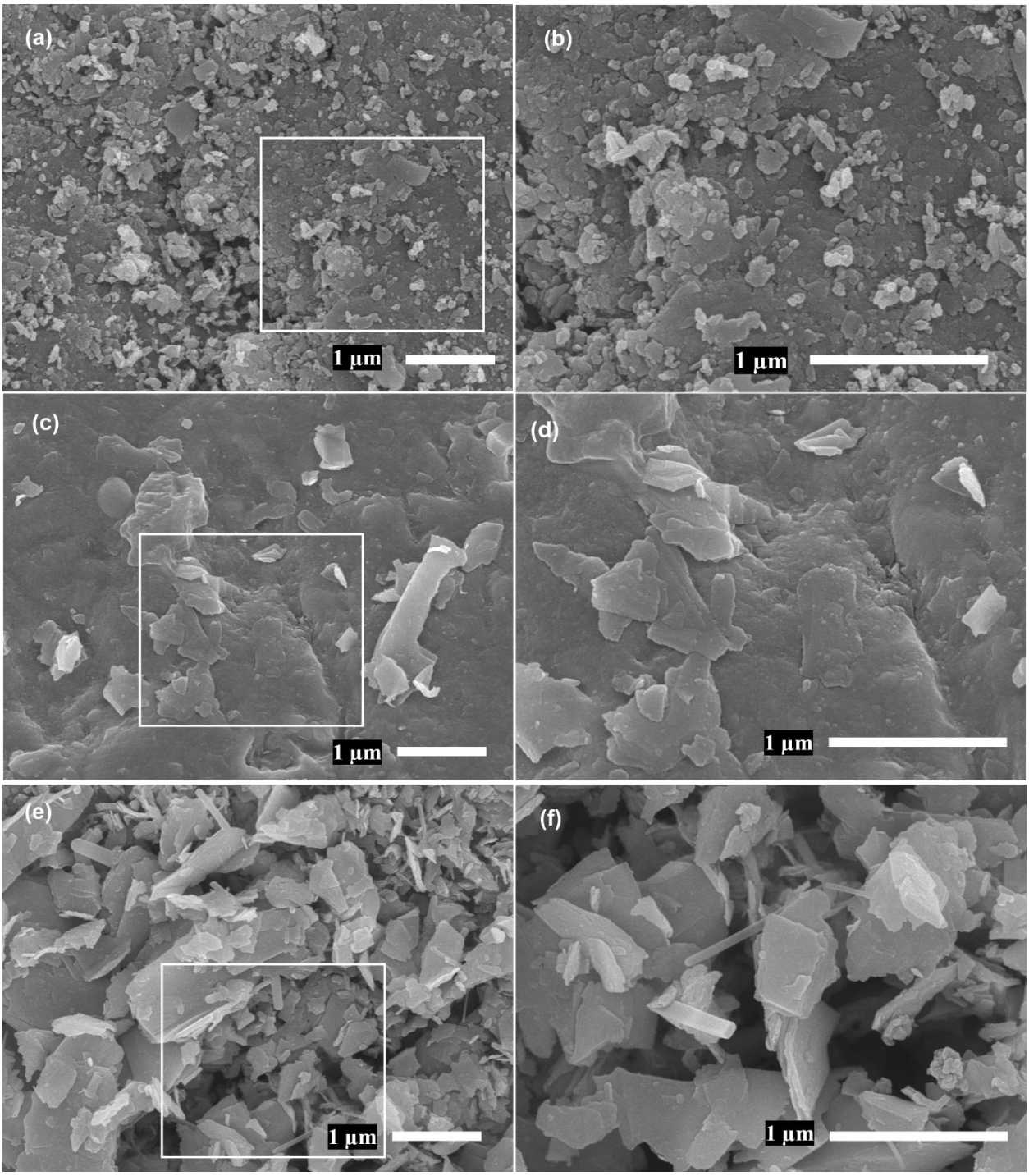

Figure 10 SEM images of Ni $(OH)_2$/NF (a, b), MoS_2/NF (c, d),75% MoS_2/NF (e, f)

Ni $(OH)_2$ microparticle is surrounded by the MoS_2 particle due to the interaction effect formed by the ball milling technique. For the nanostructured electrode **(figure 10(a, b))** irregular shape (nanoflakes) and random orientation nanosheet morphology are observed as a result of fragmentation of the micro-sized Ni $(OH)_2$ particles. The approximate size range of the nanosheets with polydisperse in lateral size dimension extends from 50 ~ 150 nm. That is lower size dispersion compared with bare MoS_2nanosheets, and that size range extends from 100 to 500 nm as shown in **figure 9(c, d),** The observed fragmentation of micron powder is attributed to the higher-pressure strike of the layered powder through NPDS with the hard substrate that accompanied by wide range sized nanostructure. It can also be shown that the fragmented particle density on the nickel foam for MoS_2 is relatively smaller compared to the fragmented particle of Ni $(OH)_2$. **Figure 10(e, f)** reveals a nanostructured $Na(OH)_2$-MoS_2 thin film with 75 wt.% MoS_2, nanosheet morphology. Due to comparative lower fragmentation and higher weight percentage, MoS_2 nanosized particles show higher uniform distribution on the composite thin film surface. Comparative small-sized Ni $(OH)_2$ particle and their ununiform distribution may reduce the ability to recognize and distinguish between the nanosized components of the heterostructure. It is supporting the results of heterostructure from XRD analysis where the presence of Ni $(OH)_2$ peaks is not revealing as MoS_2. This highly reduced $Ni(OH)_2$ nanoflakes within MoS2 nanosheet can provide a higher surface-to-volume ratio and can be effective for better electrocatalytic activity on heterostructure [57-58].

4.4 RAMAN ANALYSIS

The Raman spectra of $Ni(OH)_2$ powder and the corresponding nanostructured film is shown in **Figure 11(a, b)** respectively. The Raman spectrum of the $Ni(OH)_2$ bulk phase shows several active vibrations at 306, 445, 881, and 3582 cm^{-1}.

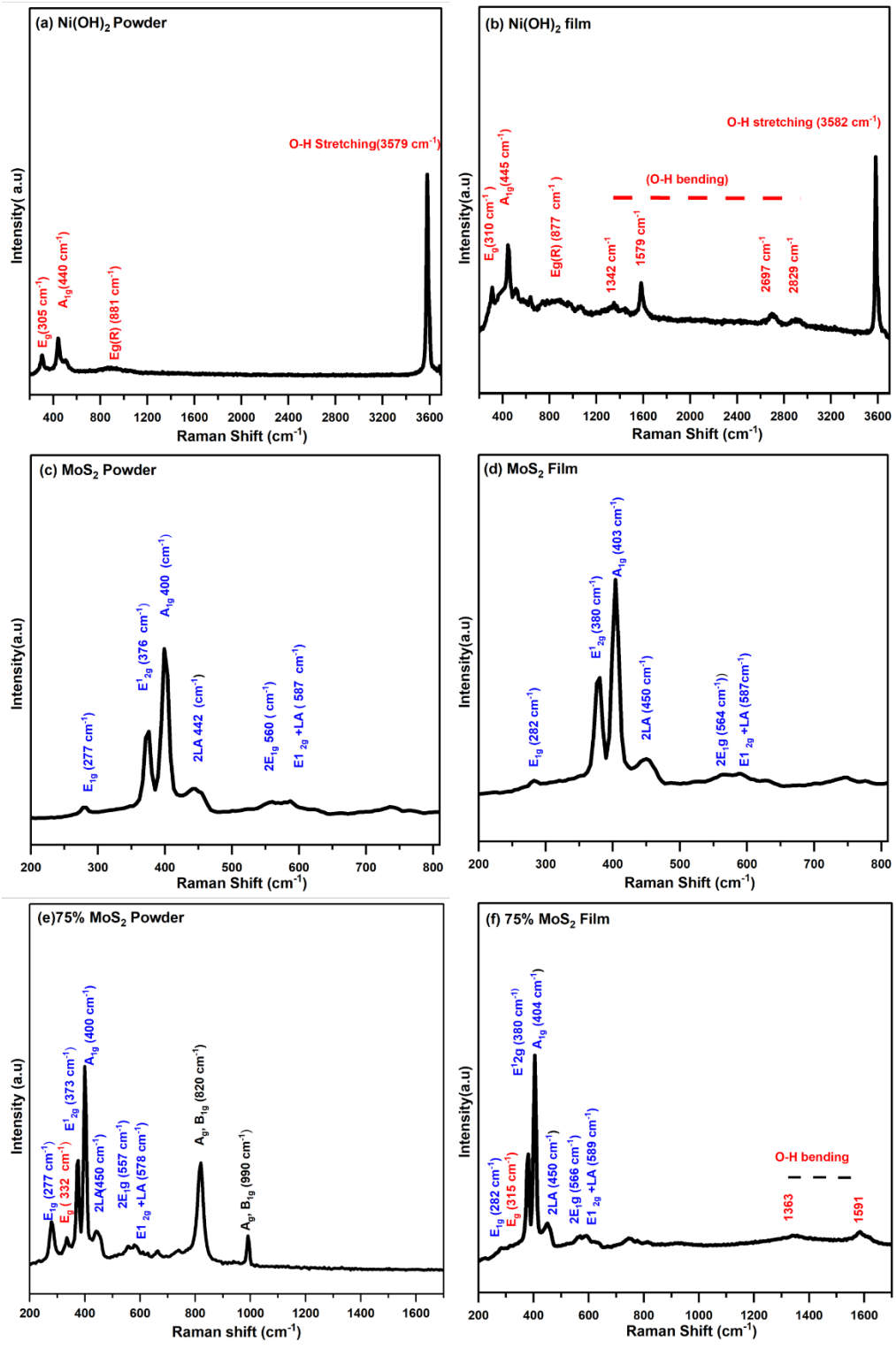

Figure 11 Raman Spectra of powder and thin film respectively. Ni $(OH)_2$ (a, b), MoS_2(c, d),75% MoS_2 (e, f)

Among these peaks, 306 and 445 are assigned to the E_g and A_{1g} symmetry modes of the bulk β-Ni $(OH)_2$ phase. The peak at 881 cm^{-1} is identified as the final lattice mode (Rotational) of the bulk β-Ni $(OH)_2$ [59-60]. For the nanostructured thin film, the active Raman vibrations associated with E_g and A_{1g} of $Ni(OH)_2$ are detected at 310 cm^{-1} and 445 cm^{-1}, respectively, as well as some extra Raman peaks recognized at 1064, 1342, 1445, 1579, 2704, and 3583 cm^{-1}. There could be an improvement in the distortion of the $Ni(OH)_2$ lattice because of the kinetic pressure induced by NPDS. Hydroxide (O-H) group shows Raman vibration at 3562 cm^{-1} due to the lattice vibration bending or stretching [61].

The Raman spectrum of MoS_2 micro flakes and the corresponding nanosheets are shown in **Figure 11(c, d),** The Raman spectrum of MoS_2 microparticles are detected at 278, 376, and 400 cm^{-1} attributed to the first-order Raman vibrations. Among these peaks, 376 cm^{-1} and 400 cm^{-1} are corresponding to the $E_1{}^{2g}$ and A_{1g} relates to the first-order vibration modes. The observed Raman peak at 278 cm^{-1} is linked to the first-order symmetry mode of $E^1{}_g$ mode. The observed Raman peaks at higher Raman shift values of 440, 560, and 587 cm^{-1} are attributed to the second-order vibrations of the longitudinal acoustic (2LA) mode, $2E_{1g}(G)$, and $E_1{}^{2g}$ (M)+LA(M), respectively [55-56]. In the case of nanostructured MoS_2 films the reported Raman are upshifted to a higher Raman shift value compared with the corresponding bulk. Raman vibration modes at 380 and 404 cm^{-1} are matched with the $E_1{}^{2g}$ and A_{1g} characteristics first order mode of the MoS_2. The 2LA (M), $2E_{1g}(G)$, and $E_1{}^{2g}$(M)+LA(M) symmetry modes produced vibrations at frequencies of 450, 564, and 592 cm^{-1}, respectively, which were identified as second-order vibration modes.

The Raman spectrum of $Ni(OH)_2$-MoS_2 composite in **Figure 11(e)** reveals several Raman peaks at 277, 332, 376, 399, 442, 557, 578, 815, and 990 cm^{-1}. These peaks are combinations and reconstructions of Ni $(OH)_2$ and MoS_2 phases powder. The Raman peak at 332 cm^{-1} is upshifted compared with pure $Ni(OH)_2$-micron powder. The peaks at 820 and 990 cm^{-1} are corresponding to the Molybdenum and oxygen (Mo=O) bonded MoO_3. The difference between these peaks belongs to the symmetry stretch and asymmetric stretch respectively [62-64]. It is possibly the effect of high powder ball milling for the interfacial and structural reconstruction of composite powder which creates new bonding [65].

Raman spectrum of $Ni(OH)_2$-MoS_2 NCs **in Figure 11(f)** reveal E_{1g} mode at 319 cm^{-1} of hexagonal $Ni(OH)_2$ that downshifted to a lower value compared to the corresponding bulk powder of Ni $(OH)_2$-MoS_2 micron powder. This result supports the XRD and SEM results that Ni $(OH)_2$ particle has experienced a high level of fragmentation and size reduction. The (Mo=O) peak is also present on the composite nanostructure at 820 cm^{1}. The two new peaks at 1363 cm^{-1} & 1691 cm^{-1} are observed which may indicate OH^- stretching and the lattice distortion same as Ni $(OH)_2$ thin film[61]. Besides, almost all MoS_2 peaks found on the composite nanostructure have been transferred to higher Raman Peak shift values. In the end, it has been observed that the bulk phase and nanostructured thin films of MoS_2 and Ni $(OH)_2$ and mixed composite were shifted to higher Raman shift values due to powder fragmentation and interlayer separation. Before deposition, lower-range crystalline domains showed lattice disorder which impacts the positive shifting [62].**Table 3** Identification of active Raman modes in the nanostructured Ni $(OH)_2$-MoS_2 heterostructure electrodes at different MoS_2 contents (wt.%).

Table. 3 Identification of active Raman modes in the nanostructured Ni $(OH)_2$-MoS_2 heterostructure electrodes at various MoS_2 Content.

Characteristics bands		Raman shift (cm^{-1})		
		MoS_2	75% MoS_2	Ni $(OH)_2$
MoS_2	E_{1g}	282	282	
	E^1_{2g}	380	380	
	A_{1g}	403	403	
	2LA(M)	450	450	
	2 E_{1g}	564	564	
	E^1_{2g}(M)+LA(M)	587	587	
Ni $(OH)_2$	E_g		315	310
	A_{1g}			445
	E_g(R)			877
	O-H stretching			3582
	O-H bending		1363, 1591	1342,1579, 2697,2829

4.5 XPS ANALYSIS

The characteristics of interfacial bonding states of nanostructured $Ni(OH)_2$, MoS_2, and $Ni(OH)_2$-MoS_2 NCs were examined using XPS. The XPS survey scans of $Ni(OH)_2$, MoS_2, and 75 wt.% MoS_2, including high-resolution XPS scans of Mo, S, O, and Ni elements have been analyzed and only the graphs with fitted peaks have been presented.

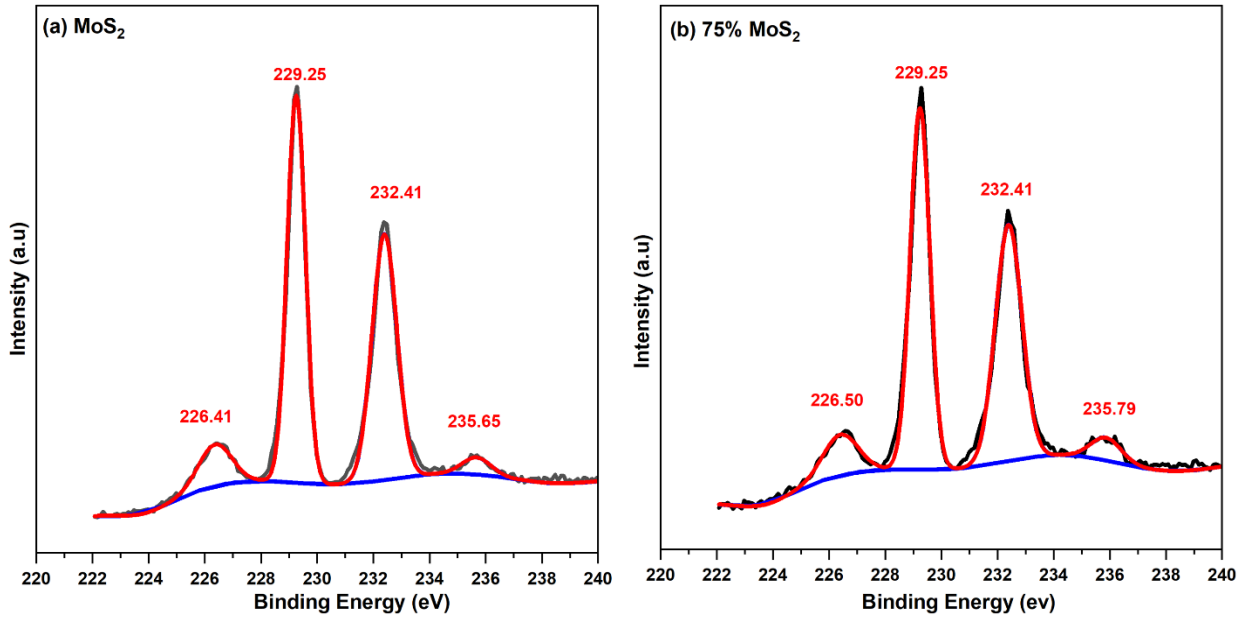

Figure 12 Deconvoluted Mo 3d XPS scan of pure MoS_2 (a), 75 % MoS_2 heterostructure

The high-resolution S 2p XPS scan of pure MoS_2 nanosheets in **(figure 15 (a))** exhibits two sub-bands, S 2p 3/2 and S 2p 1/2 at 162.13 eV and 163.28 eV, respectively. In the case of $Ni(OH)_2$-MoS_2 NCs in **Figure 15 (b)** with 75 wt.% MoS_2 similar sub-bands were seen at 162.13 eV and 163.28 eV and it indicates that there is no shifting for the case of S 2p [66-67].

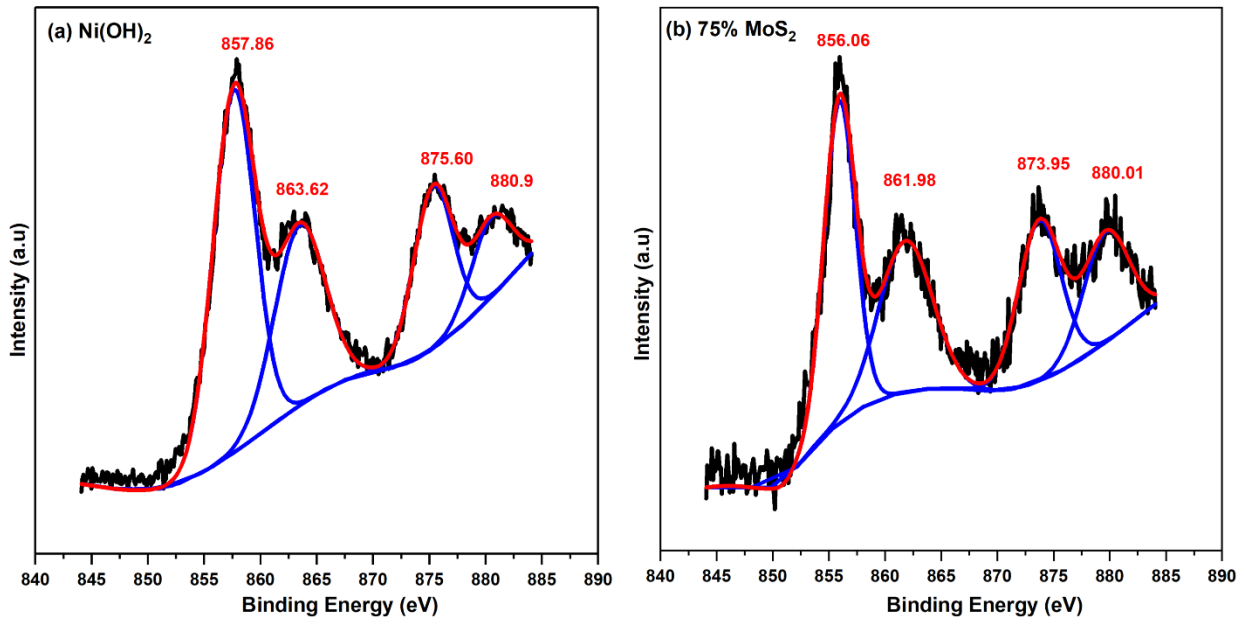

Figure 13 Deconvoluted Ni 2p XPS scan of Pure Ni $(OH)_2$(a), 75% MoS_2 heterostructure(b)

The high-resolution Mo 3d XPS scans in **Figure 12(a)** show that the binding energies of Mo 3d3/2 and Mo 3d5/2 at located at 232.41 and 229.25 eV, respectively. These bands could be attributed to Mo^{4+} in MoS_2. The peak fitting shows the characteristic of 2H-MoS_2 [68-69]. A detectable subband is found at 226.41 eV that is related to the S 2s states and frequently overlapped with the high-resolution Mo 3d states scans [69]. There is also a weak band corresponding to the high oxidation state (Mo^{6+}) at 235.65 eV [69-70]. In the case of $Ni(OH)_2$-MoS_2 NCs, the high-resolution Mo 3d XPS scan in **Figure 12(b),** exhibits that the peak corresponding to Mo^{4+} remains at the same position. However, the peaks correspond at S 2S and Mo^{6+} shifts positively to 226.50 eV and 235.79 eV, respectively.

t

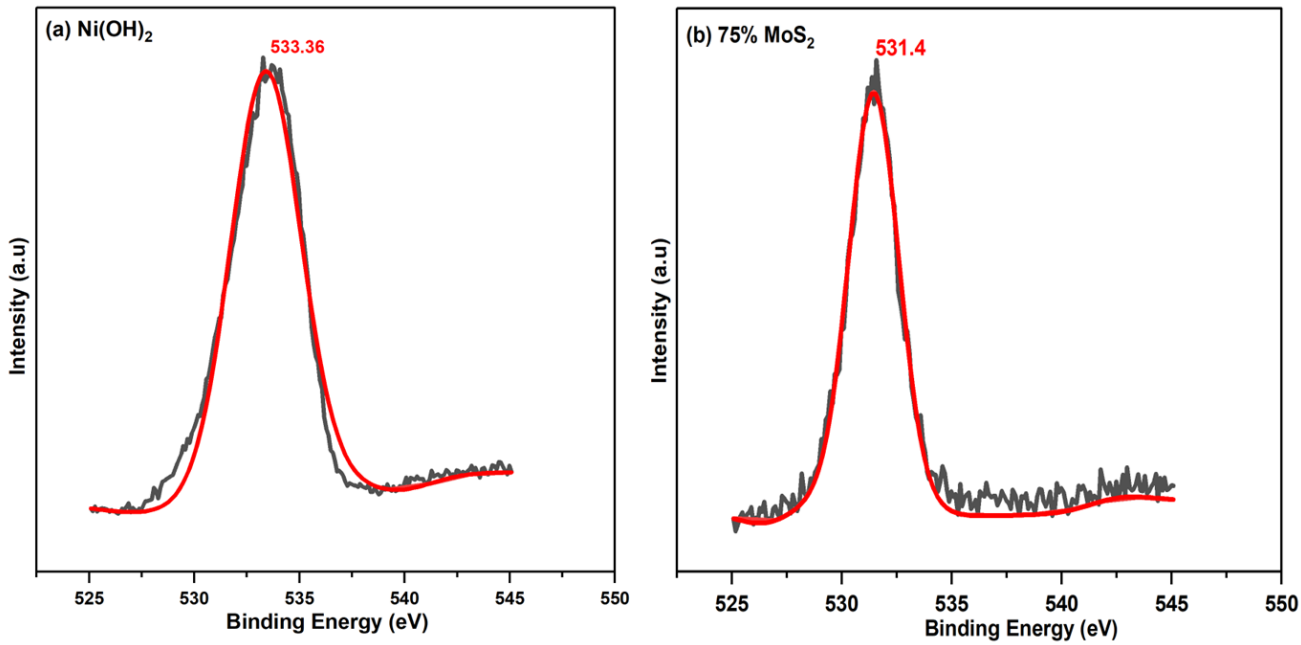

Figure 14 Deconvoluted O 1s XPS scan of pure Ni $(OH)_2$ (a), 75%MoS_2(b)

Figure 13(a, b) shows the high-resolution Ni 2p XPS scan of $Ni(OH)_2$ nanosheets and hybrid 75 wt.% MoS_2 NCs. The deconvoluted high-resolution Ni 2p XPS spectra show Ni 2p1/2 and Ni 2p3/2 showing at 857.71 and 875.48, respectively, with an energy separation of 17.77 eV. These subbands are accompanied by the satellite peak at 863.44 and 881.10 eV. This characterizes the hexagonal β-$Ni(OH)_2$ phase [71]. The deconvoluted Ni 2p peaks are negatively shifted to the lower binding energies in the case of Ni $(OH)_2$-MoS_2 hybrid NCs. This negative peak shift refers to the increase of interfacial electron density in the heterostructure electrode [72] Also, it is suggested that the improvement of electronic density to nearby Ni atoms is ascribed to the presence of interfacial Mo ions in the hybrid NCs. This process could be facilitated by an electron acceptor, which would improve the weak binding of OH* molecules to Ni centers and trigger the reactions [73].

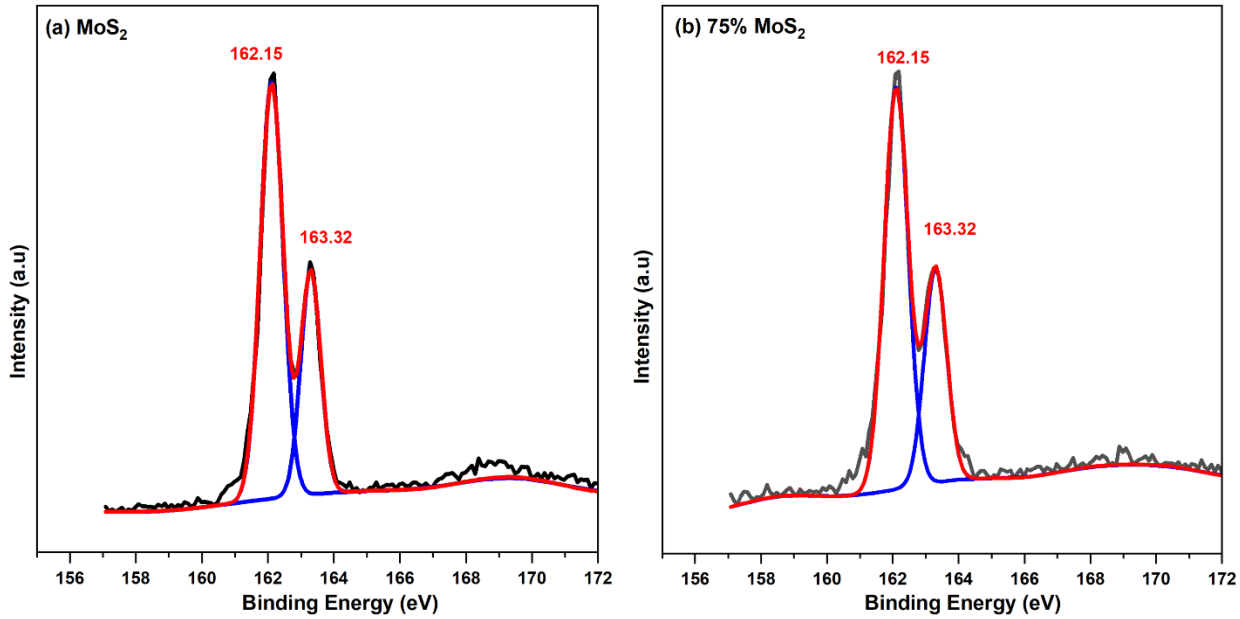

Figure 15 Deconvoluted S 2p XPS scan of pure MoS_2 (a), 75 % MoS_2 heterostructure thin film (b)

The high-resolution O 1s XPS spectra of pure Ni $(OH)_2$ and $Ni(OH)_2$-MoS_2 hybrid NCs with 75 wt.% MoS_2 are shown in **figure 14(a, b).** The high-resolution O 1 s scan of nanostructure $Ni(OH)_2$ is observed at a high binding energy of 533.61 eV in [74] that has been downshifted to 531.31 eV in the case of $Ni(OH)_2$-MoS_2 hybrid NCs with 75 wt.% MoS_2 At the interface between Transitional metal oxide and hydroxide, the analysis demonstrates synergy improvements and oxygen vacancy. Better interactions regarding heterostructure can be identified by the peak shifting of XPS. It can formulate that reconstruction of the interface and active sites can improve the electrocatalytic activity [68-69].

Table 4: XPS peaks positions estimated from the deconvolution of XPS scans

Band	Binding energy (eV)		
	MoS_2	75% MoS_2	Ni $(OH)_2$
S 2P	162.13 163.28	162.13 163.28	
Mo 3d	226.41 229.25 232.41 235.65	226.50 229.25 232.41 235.79	
O 1s		531.40	533.36
Ni 2p		855.06 861.98 873.95 880.01	857.86 863.62 875.60 880.90

CHAPTER 5

CONCLUSION

In summary, Nanosized $Ni(OH)_2$-MoS_2 thin film was fabricated with a one-step vacuum kinetic spray method from the corresponding micro-sized powder through a sustainable manufacturing route for green energy production. We produced modified working electrodes based on heterostructure $Ni(OH)_2$-MoS_2 NCs with varying different MoS_2 weight content to evaluate the electrocatalytic activity toward OER in 1.0 M KOH. Our results indicated that heterostructure $Ni(OH)_2$-MoS_2 NCs with dominating MoS_2 content provide better OER activity as a result of the reduction of charge transfer resistance. Surface analysis verified that micron particle fragmentation occurred due to the high-velocity collision of micron powder with the hard substrate. Further illustration has been drawn from Raman spectroscopy and X-Ray photoelectron spectroscopy. Raman spectroscopy confirms the lattice deformation by changing to higher Raman values in the thin film compared to micro powder. Additionally, XPS corroborates the electronic structure and density reconstruction and synergistic improvement on the interface of $Ni(OH)_2$-MoS_2.The utilized working electrode of $Ni(OH)_2$-MoS_2 hybrid NCs with 75 wt.% MoS_2 exhibited the best OER activity with a very small overpotential of 282 mV at @10 $mA{\cdot}cm^{-2}$, a very small tafel slope of 54 & long-term stability for 50 hours. Overall, the modified electrode with 75% MoS2 shows better performances than its pure phases counterparts and represents significant research in the development of efficient and sustainable electrocatalysts for green energy production.

ACKNOWLEDGEMENT

This research was supported by a National Research Foundation of Korea grant (NRF-2021R1A2C1008248), and by the “Regional Innovation Strategy (RIS)" through the National Research Foundation of Korea (NRF) funded by the Ministry of Education (MOE) (2021RIS-003)

REFERENCES

[1] G.-R. Zhang, L.-L. Shen, and D. Mei, “Enhanced electrocatalysis at ionic liquid modified solid–liquid interfaces,” Reference Module in Chemistry, Molecular Sciences and Chemical Engineering, Jan. 2023, doi: 10.1016/B978-0-323-85669-0.00022-2.

[2] P. A. Owusu and S. Asumadu-Sarkodie, “A review of renewable energy sources, sustainability issues and climate change mitigation,” http://www.editorialmanager.com/cogenteng, vol. 3, no. 1, 2016, doi: 10.1080/23311916.2016.1167990.

[3] W. Strielkowski, L. Civín, E. Tarkhanova, M. Tvaronavičienė, and Y. Petrenko, “Renewable Energy in the Sustainable Development of Electrical Power Sector: A Review,” Energies 2021, Vol. 14, Page 8240, vol. 14, no. 24, p. 8240, Dec. 2021, doi: 10.3390/EN14248240.

[4] M. Nath, A. Saxena, H. Singh, U. De Silva, W. Liyanage, and J. Masud, “(Invited) Slurry of Transition Metal Chalcogenides for Multifaceted

Electrochemical Applications: Energy Conversion, Storage, Sensing & Catalysis," ECS Meeting Abstracts, vol. MA2021-01, no. 45, p. 1769, May 2021, doi: 10.1149/MA2021-01451769MTGABS.

[5] Y. Holade et al., "Advances in Electrocatalysis for Energy Conversion and Synthesis of Organic Molecules," ChemPhysChem, vol. 18, no. 19, pp. 2573–2605, Oct. 2017, doi: 10.1002/CPHC.201700447.

[6] S. Wang, A. Lu, and C. J. Zhong, "Hydrogen production from water electrolysis: role of catalysts," Nano Converg, vol. 8, no. 1, pp. 1–23, Dec. 2021, doi: 10.1186/S40580-021-00254-X/FIGURES/16.

[7] A. Alobaid et al., "Oxygen evolution reaction (OER) mechanism under alkaline and acidic conditions," Journal of Physics: Energy, vol. 3, no. 2, p. 026001, Mar. 2021, doi 10.1088/2515-7655/ABDC85.

[8] J. J. Jarju, M. C. Figueiredo, and Y. V. Kolen'ko, "Electrocatalysis using nanomaterials," Frontiers of Nanoscience, vol. 18, pp. 343–420, Jan. 2021, doi: 10.1016/B978-0-12-820055-1.00002-2.

[9] Z. W. She, J. Kibsgaard, C. F. Dickens, I. Chorkendorff, J. K. Nørskov, and T. F. Jaramillo, "Combining theory and experiment in electrocatalysis: Insights into materials design," *Science (1979)*, vol. 355, no. 6321, Jan. 2017, doi: 10.1126/SCIENCE.AAD4998/ASSET/8E2862D5-F1CD-4F21-8F67-6708141FC3F6/ASSETS/GRAPHIC/355_AAD4998_F7.JPEG.

[10] H. Wang *et al.*, "Bifunctional non-noble metal oxide nanoparticle electrocatalysts through lithium-induced conversion for overall water splitting," *Nature Communications 2015 6:1*, vol. 6, no. 1, pp. 1–8, Jun. 2015, doi: 10.1038/ncomms8261.

[11] Y. Chen, K. Rui, J. Zhu, S. X. Dou, and W. Sun, “Recent Progress on Nickel-Based Oxide/(Oxy)Hydroxide Electrocatalysts for the Oxygen Evolution Reaction,” *Chemistry – A European Journal*, vol. 25, no. 3, pp. 703–713, Jan. 2019, doi: 10.1002/CHEM.201802068.

[12] F. Lyu *et al.*, “Noble-Metal-Free Electrocatalysts for Oxygen Evolution,” *Small*, vol. 15, no. 1, p. 1804201, Jan. 2019, doi: 10.1002/SMLL.201804201.

[13] Z.-P. Wu *et al.*, “Non-Noble-Metal-Based Electrocatalysts toward the Oxygen Evolution Reaction,” *Adv Funct Mater*, vol. 30, no. 15, p. 1910274, Apr. 2020, doi: 10.1002/ADFM.201910274.

[14] M. Yu, E. Budiyanto, and H. Tüysüz, “Principles of Water Electrolysis and Recent Progress in Cobalt-, Nickel-, and Iron-Based Oxides for the Oxygen Evolution Reaction,” *Angewandte Chemie International Edition*, vol. 61, no. 1, p. e202103824, Jan. 2022, doi: 10.1002/ANIE.202103824.

[15] Z. Yao, M. Zhu, F. Jiang, Y. Du, C. Wang, and P. Yang, “Highly efficient electrocatalytic performance based on Pt nanoflowers modified reduced graphene oxide/carbon cloth electrode,” J Mater Chem, vol. 22, no. 27, pp. 13707–13713, Jun. 2012, doi: 10.1039/C2JM31683H.

[16] M. Amiri, M. Alimoradi, K. Nekoueian, and A. Bezaatpour, “Cobalt flower-like nanostructure as modifier for electrocatalytic determination of chloropheniramine,” Ind Eng Chem Res, vol. 51, no. 44, pp. 14384–14389, Nov. 2012, doi: 10.1021/IE3016736/SUPPL_FILE/IE3016736_SI_001.PDF.

[17] Q. Zhu, Y. Qu, D. Liu, K. W. Ng, and H. Pan, “Two-Dimensional Layered Materials: High-Efficient Electrocatalysts for Hydrogen Evolution Reaction,” ACS

Appl Nano Mater, vol. 3, no. 7, pp. 6270–6296, Jul. 2020, doi: 10.1021/ACSANM.0C01331/ASSET/IMAGES/LARGE/AN0C01331_0012.JPEG.

[18] J. Cheng and D. Wang, “2D materials modulating layered double hydroxides for electrocatalytic water splitting,” Chinese Journal of Catalysis, vol. 43, no. 6, pp. 1380–1398, Jun. 2022, doi: 10.1016/S1872-2067(21)63987-6.

[19] W. Yuan, Y. Li, L. Liang, F. Wang, and H. Liu, “Dual-Anion Doping Enables NiSe2Electrocatalysts to Accelerate Alkaline Hydrogen Evolution Reaction,” ACS Appl Energy Mater, vol. 5, no. 4, pp. 5036–5043, Apr. 2022, doi: 10.1021/ACSAEM.2C00396/ASSET/IMAGES/LARGE/AE2C00396_0006.JPEG.

[20] A. Zhang, Y. Liang, H. Zhang, Z. Geng, and J. Zeng, “Doping regulation in transition metal compounds for electrocatalysis,” Chem Soc Rev, vol. 50, no. 17, pp. 9817–9844, Aug. 2021, doi: 10.1039/D1CS00330E.

[21] A. Hameed et al., “ZIF-12/Fe-Cu LDH Composite as a High Performance Electrocatalyst for Water Oxidation,” Front Chem, vol. 9, p. 379, Jun. 2021, doi: 10.3389/FCHEM.2021.686968/BIBTEX.

[22] Y. Qi et al., “A Fe3N/carbon composite electrocatalyst for effective polysulfides regulation in room-temperature Na-S batteries,” Nature Communications 2021 12:1, vol. 12, no. 1, pp. 1–12, Nov. 2021, doi: 10.1038/s41467-021-26631-y.

Y. Dou *et al.*, “Manipulating the Architecture of Atomically Thin Transition Metal (Hydr)oxides for Enhanced Oxygen Evolution Catalysis,” *ACS Nano*, vol. 12, no. 2, pp. 1878–1886, Feb. 2018, doi: 10.1021/ACSNANO.7B08691.

[23] N. Kim, D. Lim, Y. Choi, S. E. Shim, and S. H. Baeck, “Hexagonal β-Ni(OH)2 nanoplates with oxygen vacancies as efficient catalysts for the oxygen

evolution reaction," *Electrochim Acta*, vol. 324, p. 134868, Nov. 2019, doi: 10.1016/J.ELECTACTA.2019.134868.

[24] S. Li *et al.*, "Enhanced electronic interaction in hemin@Ni(OH)2 composite for efficient electrocatalytic oxygen evolution," *J Alloys Compd*, vol. 892, p. 161780, Feb. 2022, doi: 10.1016/J.JALLCOM.2021.161780.

[25] W. Guo *et al.*, "Loading FeOOH on Ni $(OH)_2$ hollow nanorods to obtain a three-dimensional sandwich catalyst with strong electron interactions for an efficient oxygen evolution reaction," *Nanoscale*, vol. 12, no. 2, pp. 983–990, Jan. 2020, doi: 10.1039/C9NR08297B.

[26] M. A. Lukowski, A. S. Daniel, F. Meng, A. Forticaux, L. Li, and S. Jin, "Enhanced hydrogen evolution catalysis from chemically exfoliated metallic MoS2 nanosheets," *J Am Chem Soc*, vol. 135, no. 28, pp. 10274–10277, Jul. 2013, doi: 10.1021/JA404523S/SUPPL_FILE/JA404523S_SI_001.PDF.

[27] M. Yu *et al.*, "Engineering Thin MoS2 Nanosheets on TiN Nanorods: Advanced Electrochemical Capacitor Electrode and Hydrogen Evolution Electrocatalyst," *ACS Energy Lett*, vol. 2, no. 8, pp. 1862–1868, Aug. 2017, doi: 10.1021/ACSENERGYLETT.7B00602/ASSET/IMAGES/LARGE/NZ-2017-00602D_0005.JPEG.

[28] J. Xie *et al.*, "Defect-Rich MoS2 Ultrathin Nanosheets with Additional Active Edge Sites for Enhanced Electrocatalytic Hydrogen Evolution," *Advanced Materials*, vol. 25, no. 40, pp. 5807–5813, Oct. 2013, doi: 10.1002/ADMA.201302685.

[29] N. Karmodak and O. Andreussi, "Oxygen Evolution on MoS2Edges: Activation through Surface Oxidation," *Journal of Physical Chemistry C*, vol. 125, no. 19, pp. 10397–10405, May 2021, doi: 10.1021/ACS.JPCC.1C02210.

[30] K. Yan and L. Yiran, “Direct Growth of MoS2 Microspheres on Ni Foam as a Hybrid Nanocomposite Efficient for Oxygen Evolution Reaction,” *Small*, vol. 12, no. 22, pp. 2975–2981, Jun. 2016, doi: 10.1002/SMLL.201600332.

[31] J. Zhang *et al.*, “Engineering water dissociation sites in MoS2 nanosheets for accelerated electrocatalytic hydrogen production,” *Energy Environ Sci*, vol. 9, no. 9, pp. 2789–2793, Aug. 2016, doi: 10.1039/C6EE01786J.

[32] A. Parija *et al.*, “Electronic structure modulation of MoS2 by substitutional Se incorporation and interfacial MoO3 hybridization: Implications of Fermi engineering for electrocatalytic hydrogen evolution and oxygen evolution,” *Chemical Physics Reviews*, vol. 2, no. 1, p. 011401, Mar. 2021, doi: 10.1063/5.0037749.

[33] X. Dai *et al.*, “Co-Doped MoS2 Nanosheets with the Dominant CoMoS Phase Coated on Carbon as an Excellent Electrocatalyst for Hydrogen Evolution,” *ACS Appl Mater Interfaces*, vol. 7, no. 49, pp. 27242–27253, Dec. 2015, doi: 10.1021/ACSAMI.5B08420/ASSET/IMAGES/LARGE/AM-2015-08420P_0008.JPEG.

[34] M. Luo, W. Sun, B. Bin Xu, H. Pan, and Y. Jiang, “Interface Engineering of Air Electrocatalysts for Rechargeable Zinc–Air Batteries,” *Adv Energy Mater*, vol. 11, no. 4, p. 2002762, Jan. 2021, doi: 10.1002/AENM.202002762.

[35] P. Zhai *et al.*, “Engineering active sites on hierarchical transition bimetal oxides/sulfides heterostructure array enabling robust overall water splitting,” *Nature Communications 2020 11:1*, vol. 11, no. 1, pp. 1–12, Oct. 2020, doi: 10.1038/s41467-020-19214-w.

[36] J. Zhang *et al.*, “Interface Engineering of MoS2/Ni3S2 Heterostructures for Highly Enhanced Electrochemical Overall-Water-Splitting Activity,” *Angewandte Chemie International Edition*, vol. 55, no. 23, pp. 6702–6707, Jun. 2016, doi: 10.1002/ANIE.201602237.

[37] B. Zhang *et al.*, “Interface engineering: The Ni(OH)2/MoS2 heterostructure for highly efficient alkaline hydrogen evolution,” *Nano Energy*, vol. 37, pp. 74–80, Jul. 2017, doi: 10.1016/J.NANOEN.2017.05.011.

[38] X. Chen *et al.*, “Facile and scalable synthesis of heterostructural NiSe2/FeSe2 nanoparticles as efficient and stable binder-free electrocatalyst for oxygen evolution reaction,” *Int J Hydrogen Energy*, vol. 46, no. 71, pp. 35198–35208, Oct. 2021, doi: 10.1016/J.IJHYDENE.2021.08.090.

[39] Y. Guan, H. Xuan, H. Li, and P. Han, “Synthesis of 3D flower-like nickel-molybdenum-sulfur microspheres as efficient and stable electrocatalyst for hydrogen and oxygen evolution reactions,” *Electrochim Acta*, vol. 320, Oct. 2019, doi: 10.1016/j.electacta.2019.134614.

[40] X. Wen *et al.*, “Creating low coordination atoms on MoS2/NiS2 heterostructure toward modulating the adsorption of oxygenated intermediates in lithium-oxygen batteries,” *Chemical Engineering Journal*, vol. 442, Aug. 2022, doi: 10.1016/j.cej.2022.136311.

[41] L. Zhang *et al.*, “Nickel Foam Supported NiO@Ru Heterostructure Towards High-Efficiency Overall Water Splitting,” *ChemPhysChem*, vol. 22, no. 17, pp. 1785–1791, Sep. 2021, doi: 10.1002/CPHC.202100317.

[42] C. Si *et al.*, "Co3[Fe(CN)6]2 nanocube derived architecture of Co,Fe co-doped MoS2 nanosheets for efficient water electrolysis," *Electrochim Acta*, vol. 309, pp. 116–124, Jun. 2019, doi: 10.1016/J.ELECTACTA.2019.04.078.

[43] K. Wang, Z. Liu, Q. Gao, N. Li, and K. Yu, "Ni(OH)2 nanoparticles decorated on 1T phase MoS2 basal plane for efficient water splitting," *Appl Surf Sci*, vol. 593, p. 153408, Aug. 2022, doi: 10.1016/J.APSUSC.2022.153408.

[44] Z. He *et al.*, "Defect-Mediated Adsorption of Metal Ions for Constructing Ni Hydroxide/MoS2Heterostructures as High-Performance Water-Splitting Electrocatalysts," *ACS Appl Energy Mater*, vol. 3, no. 7, pp. 7039–7047, Jul. 2020, doi: 10.1021/ACSAEM.0C01091/..

[45] V. Devthade and S. Lee, "Synthesis of vanadium dioxide thin films and nanostructures," *J Appl Phys*, vol. 128, no. 23, p. 231101, Dec. 2020, doi: 10.1063/5.0027690.

[46] B. Uzakbaiuly, A. Mukanova, Y. Zhang, and Z. Bakenov, "Physical Vapor Deposition of Cathode Materials for All Solid-State Li Ion Batteries: A Review," *Front Energy Res*, vol. 9, p. 213, May 2021, doi: 10.3389/FENRG.2021.625123/BIBTEX.

[47] J. Woo Park, B. Ha Kang, H. Jae Kim, J. W. Park, B. H. Kang, and H. J. Kim, "A Review of Low-Temperature Solution-Processed Metal Oxide Thin-Film Transistors for Flexible Electronics," *Adv Funct Mater*, vol. 30, no. 20, p. 1904632, May 2020, doi: 10.1002/ADFM.201904632.

[48] W. Ruythooren *et al.*, "Electrodeposition for the synthesis of microsystems," *Journal of Micromechanics and Microengineering*, vol. 10, no. 2, p. 101, Jun. 2000, doi: 10.1088/0960-1317/10/2/301.

[49] U. S. Mohanty, “Electrodeposition: A versatile and inexpensive tool for the synthesis of nanoparticles, nanorods, nanowires, and nanoclusters of metals,” *J Appl Electrochem*, vol. 41, no. 3, pp. 257–270, Mar. 2011, doi: 10.1007/S10800-010-0234-3.

[50] H. Gao *et al.*, “One-step preparation of cobalt-doped NiS@MoS2 core-shell nanorods as bifunctional electrocatalyst for overall water splitting,” *Electrochim Acta*, vol. 377, p. 138051, May 2021, doi: 10.1016/J.ELECTACTA.2021.138051.

[51] C. Qin, A. Fan, X. Zhang, S. Wang, X. Yuan, and X. Dai, “Interface engineering: few-layer MoS2 coupled to a NiCo-sulfide nanosheet heterostructure as a bifunctional electrocatalyst for overall water splitting,” *J Mater Chem A Mater*, vol. 7, no. 48, pp. 27594–27602, Dec. 2019, doi: 10.1039/C9TA10547F.

[52] A. G. Abd-Elrahim and D. M. Chun, “Kinetically induced one-step heterostructure formation of Co3O4-Ni(OH)2-graphene ternary nanocomposites to enhance oxygen evolution reactions,” *J Alloys Compd*, vol. 906, p. 164159, Jun. 2022, doi: 10.1016/J.JALLCOM.2022.164159.

[53] G. Bronoel and J. Reby, “Mechanism of oxygen evolution in basic medium at a nickel electrode,” *Electrochim Acta*, vol. 25, no. 7, pp. 973–976, Jul. 1980, doi: 10.1016/0013-4686(80)87102-7.

[54] P. Hosseini Benhangi, E. Gyenge, A. Alfantazi, Q. Liang, G. Brocks, and A. Bieberle-Hütter, “Oxygen evolution reaction (OER) mechanism under alkaline and acidic conditions,” *Journal of Physics: Energy*, vol. 3, no. 2, p. 026001, Mar. 2021, doi: 10.1088/2515-7655/ABDC85.

[55] M. M. M. Mohammed, A. G. Abd-Elrahim, and D. M. Chun, “One-step deposition of a Ni(OH)2-graphene hybrid prepared by vacuum kinetic spray for high

energy density hybrid supercapacitor," *Mater Chem Phys*, vol. 244, p. 122701, Apr. 2020, doi: 10.1016/J.MATCHEMPHYS.2020.122701.

[56] A. G. Abd-Elrahim and D. M. Chun, "Nanosized Co3O4–MoS2 heterostructure electrodes for improving the oxygen evolution reaction in an alkaline medium," *J Alloys Compd*, vol. 853, p. 156946, Feb. 2021, doi: 10.1016/J.JALLCOM.2020.156946.

[57] Q. L. Zhu and Q. Xu, "Immobilization of Ultrafine Metal Nanoparticles to High-Surface-Area Materials and Their Catalytic Applications," *Chem*, vol. 1, no. 2, pp. 220–245, Aug. 2016, doi: 10.1016/J.CHEMPR.2016.07.005.

[58] B. Qu *et al.*, "Ultrasmall Fe2O3 nanoparticles/MoS2 nanosheets composite as high-performance anode material for lithium ion batteries," *Scientific Reports 2017 7:1*, vol. 7, no. 1, pp. 1–11, Feb. 2017, doi: 10.1038/srep42772.

[59] D. S. Hall, D. J. Lockwood, C. Bock, and B. R. MacDougall, "Nickel hydroxides and related materials: A review of their structures, synthesis and properties," *Proceedings of the Royal Society A: Mathematical, Physical and Engineering Sciences*, vol. 471, no. 2174, Feb. 2015, doi: 10.1098/RSPA.2014.0792.

[60] R. A. Wahyuono *et al.*, "Structure of Ni(OH)2 intermediates determines the efficiency of NiO-based photocathodes – a case study using novel mesoporous NiO nanostars," *RSC Adv*, vol. 9, no. 67, pp. 39422–39433, Nov. 2019, doi: 10.1039/C9RA08785K.

[61] C. Murli, S. M. Sharma, S. K. Kulshreshtha, and S. K. Sikka, "High-pressure behavior of β-Ni (OH)2—A Raman scattering study," *Physica B Condens Matter*, vol. 307, no. 1–4, pp. 111–116, Dec. 2001, doi: 10.1016/S0921-4526(01)00646-9.

[22] B. C. Windom, W. G. Sawyer, and D. W. Hahn, “A raman spectroscopic study of MoS 2 and MoO 3: Applications to tribological systems,” *Tribol Lett*, vol. 42, no. 3, pp. 301–310, Jun. 2011, doi: 10.1007/S11249-011-9774-X.

[63] S. Hussain *et al.*, “Large-area, continuous and high electrical performances of bilayer to few layers MoS2 fabricated by RF sputtering via post-deposition annealing method,” *Scientific Reports 2016 6:1*, vol. 6, no. 1, pp. 1–13, Aug. 2016, doi: 10.1038/srep30791.

[64] D. Di Yao, J. Z. Ou, K. Latham, S. Zhuiykov, A. P. O’Mullane, and K. Kalantar-Zadeh, “Electrodeposited α- And β-phase MoO 3 films and investigation of their gasochromic properties,” *Cryst Growth Des*, vol. 12, no. 4, pp. 1865–1870, Apr. 2012, doi: 10.1021/CG201500B.

[65] S. Namba, A. Takagaki, K. Jimura, S. Hayashi, R. Kikuchi, and S. Ted Oyama, “Effects of ball-milling treatment on physicochemical properties and solid base activity of hexagonal boron nitrides,” *Catal Sci Technol*, vol. 9, no. 2, pp. 302–309, Jan. 2019, doi: 10.1039/C8CY00940F.

[66] J. Zhang *et al.*, “Interface Engineering of MoS2/Ni3S2 Heterostructures for Highly Enhanced Electrochemical Overall-Water-Splitting Activity,” *Angewandte Chemie International Edition*, vol. 55, no. 23, pp. 6702–6707, Jun. 2016, doi: 10.1002/ANIE.201602237.

[67] A. Muthurasu, V. Maruthapandian, and H. Y. Kim, “Metal-organic framework derived Co3O4/MoS2 heterostructure for efficient bifunctional electrocatalysts for oxygen evolution reaction and hydrogen evolution reaction,” *Appl Catal B*, vol. 248, pp. 202–210, Jul. 2019, doi: 10.1016/J.APCATB.2019.02.014.

[68] G. Tai *et al.*, “Fast and large-area growth of uniform MoS2 monolayers on molybdenum foils,” *Nanoscale*, vol. 8, no. 4, pp. 2234–2241, Jan. 2016, doi: 10.1039/C5NR07226C.

[69] B. Li *et al.*, “Preparation of Monolayer MoS2 Quantum Dots using Temporally Shaped Femtosecond Laser Ablation of Bulk MoS2 Targets in Water,” *Scientific Reports 2017 7:1*, vol. 7, no. 1, pp. 1–12, Sep. 2017, doi: 10.1038/s41598-017-10632-3.

[70] Y. Yang *et al.*, “MoS2-Ni3S2 Heteronanorods as Efficient and Stable Bifunctional Electrocatalysts for Overall Water Splitting,” *ACS Catal*, vol. 7, no. 4, pp. 2357–2366, Apr. 2017, doi: 10.1021/ACSCATAL.6B03192/ASSET/IMAGES/LARGE/CS-2016-031922_0006.JPEG.

[71] S. Min, C. Zhao, Z. Zhang, G. Chen, X. Qian, and Z. Guo, “Synthesis of Ni(OH)2/RGO pseudocomposite on nickel foam for supercapacitors with superior performance,” *J Mater Chem A Mater*, vol. 3, no. 7, pp. 3641–3650, Feb. 2015, doi: 10.1039/C4TA06233G.

[72] C. Zhao *et al.*, “Electrostatic force-driven anchoring of Ni(OH)2 nanocrystallites on single-layer MoS2 for high-performance asymmetric hybrid supercapacitors,” *Electrochim Acta*, vol. 320, p. 134591, Oct. 2019, doi: 10.1016/J.ELECTACTA.2019.134591.

[73] G. Tian *et al.*, “Hierarchical NiMoP2-Ni2P with amorphous interface as superior bifunctional electrocatalysts for overall water splitting,” *J Mater Sci Technol*, vol. 77, pp. 108–116, Jun. 2021, doi: 10.1016/J.JMST.2020.09.046.

[74] A. G. Abd-Elrahim and D. M. Chun, “Kinetically induced one-step heterostructure formation of Co3O4-Ni(OH)2-graphene ternary nanocomposites to enhance oxygen evolution reactions,” *J Alloys Compd*, vol. 906, p. 164159, Jun. 2022, doi: 10.1016/J.JALLCOM.2022.164159.

BIBLIOGRAPHY